Deciphering the role of optimal P2/O3 phase fraction in enhanced cyclability and specific capacity of layered oxide cathodes

Samriddhi Saxena[a], Manish Badole[a], Hari Narayanan Vasavan[a], Velaga Srihari[b],
Asish Kumar Das[a], Pratiksha Gami[a], Sonia Deswal[c], Pradeep Kumar[c], Sunil Kumar[a,*]

[a] *Department of Metallurgical Engineering and Materials Science, Indian Institute of Technology Indore, Simrol, 453552, India*

[b] *High Pressure & Synchrotron Radiation Physics Division, Bhabha Atomic Research Centre, Mumbai, 400085, India*

[c] *School of Physical Sciences, Indian Institute of Technology Mandi, Mandi, 175005, India*

[*] *E-mail: sunil@iiti.ac.in*

Abstract

Poor cyclability and rate performance of layered oxide cathodes have impeded their deployment in Na^+ batteries. Here, Mn-rich biphasic cathodes with tuned P2/O3 phase fractions were synthesized by varying Na in $Na_xMn_{0.60}Ni_{0.30}Cu_{0.10}O_2$ (NMNC-x) ($0.80 \leq x \leq 1.00$) and the P2/O3 phases were confirmed using X-ray diffraction (XRD), X-ray photoelectron spectroscopy, and extended X-ray absorption fine structure spectroscopy. The Rietveld refinement of XRD data showed that the O3 phase fraction increased from 13% to 89% with increasing x from 0.80 to 1.00. The NMNC-0.90 sample (with 54% O3 phase) demonstrated excellent rate performance (119 and 100 mAh g^{-1} at 1C and 3C, respectively) but poor cyclic stability (64% capacity retention at 1C after 200 cycles). P2 dominant NMNC-0.80 showed exceptional rate performance (147 & 103 mAh g^{-1} at 0.1C & 3C, respectively) and O3 dominant NMNC-1.00 exhibited a high specific capacity (187 mAh g^{-1} at 0.1C). These cathodes showed excellent capacity retention of around 91% at 1C after 200 cycles. *Operando* Synchrotron XRD results confirmed a reversible O3↔P3 phase transformation at ~3.4 V. Further, a significant mismatch in the levels of the strain developed in the P2 and O3 phases was observed in NMNC-0.90 sample during charge/discharge, explaining its poor cyclability. Na^+ diffusion coefficients calculated from the galvanostatic intermittent titration technique were in the 10^{-12} - 10^{-10} cm^2 s^{-1} range. This investigation shed light on the optimum P2/O3 phase fraction for designing biphasic cathodes with high specific capacity and cyclability.

Keywords: P2/O3 cathodes; Cyclic stability; Lattice strain; Phase transformation; *Operando* Synchrotron XRD.

1. Introduction

The intermittent and unstable nature of renewable energy sources has necessitated the development of efficient energy storage systems. Owing to the high energy density and long cycle life, secondary batteries have emerged as one of the most efficient means of energy storage. Lithium-ion batteries (LIBs) have emerged as the dominant electrochemical energy storage devices; however, their extensive use is constrained due to high costs and limited lithium resources. The widespread availability of sodium (Na) sources makes the sodium-ion system affordable and sustainable, making Na-ion batteries (NIBs) the most sought-after option to replace Li-ion batteries [1-6].

Several cathode materials have been investigated for Na-ion batteries, such as *layered oxides*, *polyanionic compounds*, and *Prussian blue analogues* [7-9]. However, layered Na-transition metal (TM)-oxides (Na_xTMO_2) have a performance edge over other potential cathodes in terms of simplicity of synthesis and excellent Na-storage capacity. Additionally, layered TM oxides can take on a variety of structural forms depending on the crystallographic site (octahedral: O, or prismatic: P) where the Na-ions are located in the Na layer as well as the number (n) of distinct stacking sequences of TMO_6 slab before repeating itself (typically, n = 2-3). The P2, P3, and O3-type layered oxides (LOs) have been extensively researched for their structural and electrochemical properties [10-13]. The typical LOs for NIB cathode materials based on Mn/Ni have good specific capacity and rate capability, making them a suitable cathode material choice

[14]. Based on the Ni^{2+}/Ni^{4+} redox process, this system shows a high specific capacity, whereas the electrochemically inactive Mn^{4+} could help maintain structural stability. However, these materials usually experience an irreversible phase transition during charge-discharge that causes structural alteration, volume change, and capacity deterioration [13, 15]. Furthermore, the inclusion of Cu ions in the transition metal layers is reported to improve various properties, including moisture stability, cyclability, and nominal voltage in layered oxides [16-18]. Recent advances in the $Na_x(Mn\text{-}Ni\text{-}Cu)O_2$ system have demonstrated a specific capacity of ~90 mAh g^{-1}, a nominal voltage of ~3.4 V, and capacity retention of over 80% after 200 cycles at 0.1C [19].

Due to the P2-type layered structure's open channel diffusion, the migration of Na-ions has a low energy barrier; As a consequence, these materials exhibit superior cycling stability and high Na^+ conductivity. A conventional P2-type $Na_{2/3}Ni_{1/3}Mn_{2/3}O_2$ material delivers a reversible specific capacity of 160 mAh g^{-1} in the 2.0 - 4.5 V range, but an irreversible P2 to O2 phase transition beyond 4.2 V resulted in a 20% volume change and capacity fading [20]. The P2-O2 single-phase transition during Na^+ insertion and extraction can be inhibited or converted to a highly reversible P2-OP4 process by efficient structural design techniques. Another disadvantage of the P2-type phases, compared to the O3-type, is lower specific capacity and higher initial irreversible capacity loss owing to the lower sodium content. Accordingly, O3-type cathodes typically exhibit higher energy density, specific capacity, and better anode material matching in Na-ion full cells. On the other hand, Na^+ ions must overcome a significant energy barrier by sharing an edge with the next tetrahedral site when moving from one octahedral site to another in O3-type layered oxides, resulting in reduced ionic conductivity in these phases. The O3-type $NaNi_{1/2}Mn_{1/2}O_2$, with Ni^{2+} and Mn^{4+}, delivered a reversible specific capacity of 200 mAh g^{-1} in the 2.2 – 4.5 V range [21]. Nonetheless, to prevent the significant capacity degradation caused by charging beyond 4.0 V, the usable capacity of the full cell was restricted to 120 mAh g^{-1} in the 2.2 – 3.8 V range.

One of the ways to stabilize the crystal structure during charge-discharge cycling is voltage limitation at the expense of usable specific capacity. The incorporation of electrochemically inactive ions (Mg [22, 23], Li [24, 25], Zn [26, 27], etc. [16, 18, 28]) to act as pillar ions in the transition metal layer is another method to improve the cyclability of the layered oxides. For example, a P2-type $Na_{0.67}Mn_{0.6}Ni_{0.2}Cu_{0.1}Mg_{0.1}O_2$ cathode material exhibits 70.7% specific capacity retention after 200 cycles [29]. Another recent Cu/Ti co-doped P2-type Fe/Mn-based layered oxide cathode showed an excellent reversible capacity of 130 mAh g^{-1} at 0.1C and 71.1% specific capacity retention after 300 cycles at 5C [30]. A Li-substituted O3-type $NaLi_{0.1}Ni_{0.35}Mn_{0.55}O_2$ cathode shows improved electrochemical performance after Li^+ incorporation [31]. Another study by Yu et al. reports an O3-type cathode with a capacity retention of 82% after 200 cycles [32].

Recently, numerous studies have been carried out on various compositions in the $Na_xMn_{1-y}M_yO_2$ (where M is a combination of transition metal cations) system with mixed phases to enhance their electrochemical performance [33-40]. For instance, Guo et al. reported a P2/O3-$Na_{0.66}Li_{0.18}Mn_{0.71}Ni_{0.21}Co_{0.08}O_2$ with a P2:O3 weight ratio of 94:6, which delivers a discharge capacity of 200 mAh g^{-1} at a current density of 10 mA g^{-1} in the 1.5-4.5 V voltage range [41]. A multi-ion doped P2/O3 $Na_{0.9}Ni_{0.2}Mn_{0.55}Cu_{0.14}Ti_{0.07}Zn_{0.04}O_2$ prepared by Wang et al. exhibited a discharge capacity of 133.9 mAh g^{-1} at 0.1C and a notable structure stability with 78.9% capacity retention after 500 cycles at 10C [42]. Another study by Ding et al. reported a biphasic $Na_{0.67}Li_{0.15}Ni_{0.18}Mg_{0.02}Mn_{0.8}O_2$ prepared by introducing the O3 structure into the P2 structure and controlling the weight fraction by varying the sintering temperature. The material with 4.2 wt.% of the P2 phase and 95.8 wt.% of the O3 phase displayed a discharge capacity of 160 mAh g^{-1} at 0.1 C in the 1.5-4.2 V range and a 70% of initial capacity retention after 100 cycles [43]. By introducing Li in P2-$Na_{0.67}Fe_{0.25}Mn_{0.75}O_2$, Wang et al. demonstrated the effect of P2/O3 biphasic structure in successfully reducing the crucial Jahn-Teller distortion and preventing the irreversible phase transition in $Na_{0.67}Li_{0.2}Fe_{0.2}Mn_{0.6}O_2$ [33]. M. Alam et al. controlled the phase fraction of P2/O3 by modifying the cooling rate, and P2/O3-$Na_{0.7}MnO_2$ with a ratio of 68:32 (wt.%, P2:O3) showed an initial discharge capacity of 171 mAh g^{-1} and an improved rate-capability (76 mAh g^{-1} at 10C) [44]. A P2/O3-$Na_{0.8}Mn_{0.55}Ni_{0.25}Fe_{0.1}Ti_{0.1}O_2$ cathode with superior rate performance and higher energy density than either of the P2 and O3 phases between 1.5 and 4.3 V was synthesized by Wang et al. by tuning the ratio of Mn and Ni [19]. The material exhibited a reversible capacity of 154.6 mAh g^{-1} with ~ 100% coulombic efficiency and capacity retention of 80.2% after 100 cycles at 0.1C. These studies reveal the superiority of biphasic cathodes over their single-phase counterparts.

Herein, a series of P2/O3 $Na_xMn_{0.60}Ni_{0.30}Cu_{0.10}O_2$ (x = 0.80, 0.85, 0.90, 0.95, and 1.00) (NMNC-x) cathodes were designed with varying P2/O3 phase fractions and compare the electrochemical properties of biphasic structures with the domination of either phase to the material with equal phase fractions of P2 and O3 phase. The changes in the crystal structure at various states of charge induced by different phases are quantified by refinement of the *operando* Synchrotron XRD data. Various reports on biphasic cathodes have highlighted the synergy between the phases, leading to an *interlocking effect* causing enhancement in their electrochemical properties. Contrary to this, poor cyclability was obtained for the sample with an almost equal fraction of P2 and O3 phases (NMNC-0.90). A systematic study of the electrochemical properties showed improved cyclability, which is attributed to the lesser mismatch in the levels of the strain at P2/O3 interfaces during sodium extraction/insertion in O3/P2-dominant samples. These findings would attract the attention of researchers working on Na-ion batteries and further extend the discussion on the role of phase fractions in enhancing the cyclability and specific capacity of biphasic layered oxide cathodes.

2. Experimental

The biphasic $Na_{0.80}Mn_{0.60}Ni_{0.30}Cu_{0.10}O_2$, $Na_{0.85}Mn_{0.60}Ni_{0.30}Cu_{0.10}O_2$, $Na_{0.90}Mn_{0.60}Ni_{0.30}Cu_{0.10}O_2$, $Na_{0.95}Mn_{0.60}Ni_{0.30}Cu_{0.10}O_2$, $Na_{1.00}Mn_{0.60}Ni_{0.30}Cu_{0.10}O_2$, materials were synthesized using the conventional sol-gel method. Precursors of copper (copper (II) nitrate trihydrate), manganese (manganese (II) acetate tetrahydrate), nickel (nickel (II) acetate tetrahydrate), and sodium (sodium carbonate) were dissolved in deionized water and stirred for 8 h. Table S1 gives the exact amounts of precursors used (in g) to obtain 10g of the final products for different x. To this, ethylene glycol and citric acid were added in appropriate ratio, and the mixture continued to stir for 12 h to create a homogeneous solution. A gel was obtained by heating this solution to around 80 °C. The dry gel was ground prior to a 12 h heat treatment at 600 °C. The resulting powders were calcined in air for 12 h at 900 °C to form the final product. These calcined powders were labeled as NMNC-x; x denotes the sodium content = 0.80, 0.85, 0.90, 0.95, and 1.00.

The synthesized compounds were examined for their phase structure using room temperature X-ray diffraction technique (XRD) in 2θ range of 10°- 80° using an Empyrean, Malvern Pananalytical diffractometer with Cu-K_α radiation. Further, Rietveld refinement was performed on the XRD data, and the corresponding crystallographic parameters of the NMNC-x samples were calculated using the *TOPAS Academic* (version 6) software package [45]. The Mn *K*-edge extended X-ray absorption fine structure spectroscopy (EXAFS) was carried out using the scanning EXAFS beamline (BL-9) at the Indus-2 synchrotron source (2.5 GeV, 150 mA) at Raja Ramanna Centre for Advanced Technology (RRCAT), Indore, India. Inductively coupled plasma atomic emission spectrometry (ICP-AES) (SPECTRO Analytical Instruments GmbH, Germany, Model: ARCOS, Simultaneous ICP Spectrometer) was used to determine the specific chemical compositions of the prepared cathode materials. Energy-dispersive X-ray spectroscopy (EDS) equipped field emission scanning electron microscope (SEM) (model

JEOL-7610) was used to investigate the morphology and elemental distribution in the powder materials. X-ray photoelectron spectroscopy (XPS) measurements were done on the as-prepared powder samples and the cycled cathodes to verify the oxidation states of the constituent transition metal cations present in NMNC-*x* samples using a Thermofisher Scientific (Naxsa base) equipped with a 1486.6 eV (Al Kα) X-ray source. For ex-situ XPS studies, the coated cathodes were taken from the de-crimped coin-cells at different states of charge.

Electrochemical tests were performed with CR-2032-coin cells fabricated with NMNC-*x* as the working electrode, sodium metal as the counter & reference electrode, Whatman GF/D as the separator, and 1M $NaClO_4$ in a 1:1 volume ratio of EC-PC (ethylene carbonate – propylene carbonate) as the electrolyte. For cathode preparation, the 80:10:10 weight ratio of active material, PVDF binder, and Ketjen black were mixed in N-methyl pyrrolidone (NMP) solvent. After coating an Al current collector with the prepared slurry, it was dried at 120 °C for 8 hours in a vacuum oven before being punched into disks of 16 mm diameter. The active material mass loading was ~ 2-3 mg cm^{-2}, and an apparent active mass density of ~ 1.5-2.0 g cm^{-3}. The prepared coin cells were subjected to cyclic voltammetry (CV) tests between 2.0 V and 4.2 V with a scan rate of 0.1 mV s^{-1} using a Keithley source meter unit (Model 2450-EC). Galvanometric charge-discharge (GCD) tests were performed on the coin cells using a Neware Battery Tester (Model no. CT-4008T) between 2.0 V and 4.2 V. The cathode material was evaluated for its rate performance at 0.1C, 0.2C, 0.5C, 1C, 2C, and 3C, and the cyclability measurements were done at 1C for 200 cycles between 2.0 - 4.2 V. The sodium-ion diffusion coefficient of the half-cells was estimated using the galvanostatic intermittent titration technique (GITT) performed on the Neware battery tester equipment. For the fabrication of full cell, hard carbon was used as the anode (coated on aluminium foil with 80 wt.% hard carbon, 10 wt.% Ketjen black, and 10 wt.% PVDF). Hard carbon electrode was sodiated and de-sodiated electrochemically in a sodium metal half-cell configuration prior to its use as the negative electrode in NMNC-1.00–hard carbon full cell.

The phase transformations that occurred during electrochemical cycling were investigated by operando studies carried out using extreme conditions – angle dispersive/energy dispersive synchrotron X-ray diffraction (BL11) at Indus-2 beamline (RRCAT) with a beam wavelength of 0.8312 Å and beam energy of 2.5 GeV. The coin cells for the operando studies were prepared by drilling 3 mm holes in the top & bottom cap of the CR2032 coin-cell casing to allow the beam to pass through the cell. A Kapton tape was used to cover the drilled holes in coin cell casings to prevent environmental exposure.

3. Results and Discussion

3.1. XRD

The room temperature XRD patterns and the phase evolution obtained for $Na_xMn_{0.60}Ni_{0.30}Cu_{0.10}O_2$ (NMNC-x) calcined at 900 °C are shown in Fig. 1(a) and confirm the biphasic formation in all samples. All the diffraction peaks can be matched with the P2 phase ($Na_{0.7}MnO_2$-type, JCPDS # 27-0571) and the O3 phase (α-$NaFeO_2$ type, JCPDS # 82-1495) [46]. This is consistent with the previous reports on Na_xTMO_2 layered oxides, where both P2 and O3 phases are reported [47-49]. It is evident from Fig. 1(a1-a2) that the peak intensities of the (003) and (104) distinguishing peaks for O3 increase with increasing Na content, while the (002) and (102) distinguishing peaks for P2 decrease. The preliminary analysis of XRD data suggests a continuous increase in the O3 phase fraction with increasing Na in NMNC-x. To further analyze the effect of varying sodium content (x) and calcination temperature (T) on the phase fractions, several samples were prepared in the $Na_xMn_{0.60}Ni_{0.30}Cu_{0.10}O_2$ system by varying x & T, and the results are summarized in Table S2.

Further, the P2/O3 phase fractions and the lattice parameters of the NMNC-*x* samples (calcined at 900 C) were determined by performing the Rietveld refinement on the XRD data. The fitted XRD patterns, experimental data, difference curves, and Bragg positions of corresponding space groups are shown in Fig. 1(b) and Fig. S1(a, b, c, and d). The detailed structural and crystallographic parameters obtained from the refinement are consolidated in Table 1 and Tables S3-S7, respectively. This XRD data provide confirmation and quantification of P2 and O3 phases in these samples.

The phase evolution graph (Fig. 1(c)) represents an increase in the O3 phase fraction from 13% to 89% with increasing Na content from $x = 0.80$ to $x = 1.00$. Interestingly, the peak intensity ratio of the major peaks of the P2 O3 phases can be used to estimate the phase fractions in the prepared NMNC-*x* samples. The phase percentage (ρ) can be estimated from the following formula:

$$\rho = \frac{I_{P2(002)}}{I_{O3(003)} + I_{O3(104)}} \times 100 \qquad (1)$$

where ρ is the phase percentage, $I_{P2(002)}$ is the peak intensity of (002) peak of P2, and $I_{O3(003)}$ & $I_{O3(104)}$ are the peak intensities of (003) & (104) peaks of O3. It can be observed from Fig. S2 that the phase percentages estimated by the intensity method (ρ) are similar to the values obtained by the Rietveld refinement of the XRD data. While detailed Rietveld refinement would provide more accurate values, a simple XRD peak intensities ratio could also be used to estimate the P2 and O3 phase fractions in these materials.

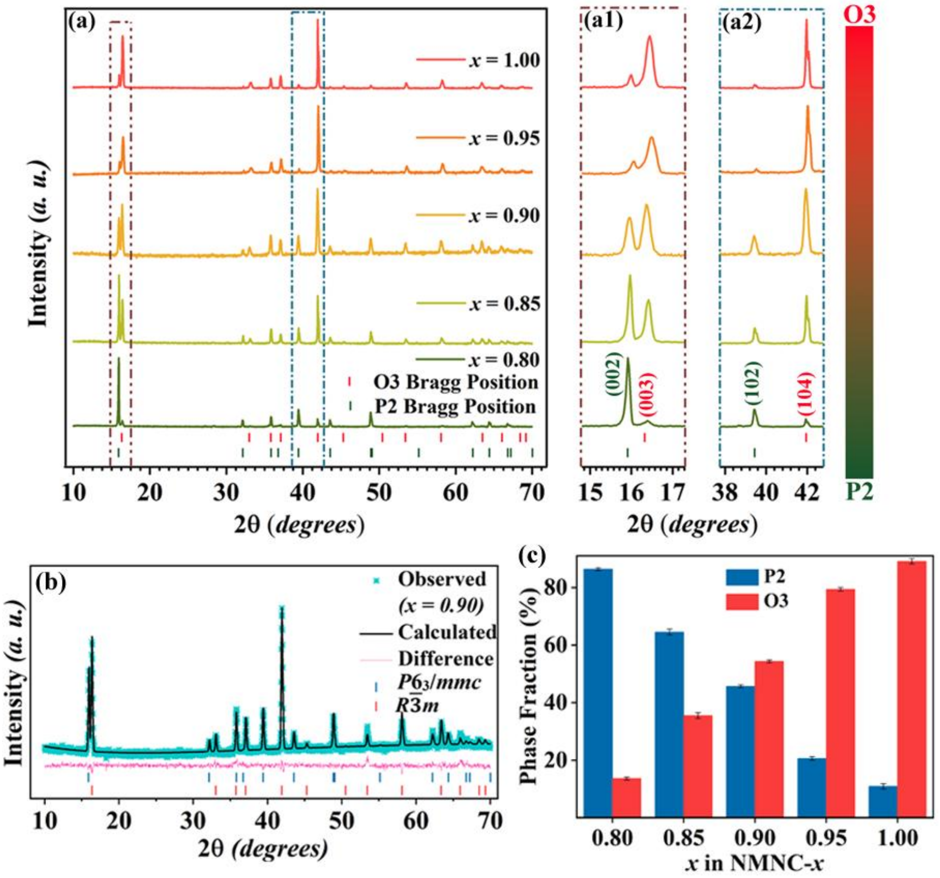

Fig. 1. (a) Room temperature XRD patterns of NMNC-*x* (0.08 ≤ *x* ≤ 1.00) samples showing the coexistence of P2 and O3 phases. Magnified view of (a1) P2 (002) & O3 (003) peaks, and (a2) P2 (102) & O3 (104) peaks showing the phase evolution from P2 to O3 with increasing Na content. (b) Rietveld refinement profile of XRD data for NMNC- 0.90. (c) Phase evolution graph showing P2 and O3 phase fractions at various Na contents.

The refinement of XRD data suggests that all the peaks can be ascribed to the $P6_3/mmc$ space group for the P2-type structure and the $R\overline{3}m$ space group for the O3-type structure with hexagonal symmetries. The two minor peaks at 27.2° and 28.4° in the XRD patterns of NMNC-0.80 and NMNC-0.85 (Fig. S1(a & b)) are a result of Na-ion vacancy ordering induced superlattice reflections, which is a well-known phenomenon in layered oxides [50-52]. The Na-ion vacancy ordering peaks disappear with increasing *x* in NMNC-*x* from 0.90 to 1.00. A comparison of the lattice parameters of the biphasic compounds shows a decrease in the lattice parameter *c* of both phases with an increase in Na content from 0.80 to 1.00. This is induced by the greater screening effect of Na^+, which results in lower O^{2-} - O^{2-} coulombic repulsions. The XRD refinement data was used to visualize the crystal structures of the P2 and O3 phases using VESTA software, as shown in Fig. S1(e) [53]. The conduction pathways (indicated by black arrows) show that the Na^+ migration in P-type layered oxides occurs directly from one prismatic site to another via rectangular bottlenecks. On the other hand, sodium-ion movement in O-type layered oxides occurs from one octahedral site to the adjacent tetrahedral site and then to the following octahedral site *via* triangular bottlenecks. Such a migration of Na ions through the small tetrahedral sites is expected to have a detrimental impact on the rate performance of the NMNC-0.95 and NMNC-1.00 cathodes.

Table 1 Lattice parameters and R-factors of P2/O3 NMNC-*x* samples obtained from the Rietveld refinement.

Sample NMNC-*x*	***Phase***	***a*** **(Å)**	***c*** **(Å)**	***V*** **(Å^3)**	R_{wp}, R_{exp}, R_p, ***GOF***
x = 0.80	P2	2.8932(1)	11.1367(6)	80.79(1)	3.47, 2.18, 2.56, 1.59
	O3	2.9343(2)	16.252(2)	121.04(2)	
x = 0.85	P2	2.8936(2)	11.1356(1)	80.72(1)	3.53, 2.91, 2.76, 1.21
	O3	2.9347(2)	16.248(1)	121.15(2)	
x = 0.90	P2	2.8941(1)	11.1349(7)	80.85(1)	3.22, 2.17, 2.37, 1.48
	O3	2.9350(1)	16.245(1)	121.01(1)	
x = 0.95	P2	2.8934(5)	11.1347(2)	80.73(3)	4.45, 2.69, 3.18, 1.65
	O3	2.9345(3)	16.244(2)	121.06(3)	
x = 1.00	P2	2.8945(4)	11.1342(2)	80.75(2)	3.19, 2.20, 3.21, 1.45
	O3	2.9349(1)	16.236(1)	121.14(1)	

The local structure of the NMNC-*x* materials was further probed with extended X-ray absorption fine structure (EXAFS) spectra of the as-prepared cathode powders. Fig. S3 shows the Fourier transforms of Mn *K*-edge spectra of NMNC-0.80 and NMNC-1.00. The blue dashed lines indicate the radial distance limits within which the fit was carried out. In Fig. S3(a) and (b), the first peak at ~ 1.46 Å originates from Mn-O co-ordination, while the second peak at ~ 2.52 Å results from Mn-TM & Mn-Na single scattering. The values of Mn-O and Mn-Na distances predicted from the EXAFS fitting match well with those calculated from the Rietveld refinement of the XRD data.

The elemental ratio calculated from ICP-AES are given in Table S8. The Mn/Ni/Cu content remains almost invariant, whereas Na content increases expectedly with an increase in *x*. The overall compositions of the samples are in good agreement with the nominal compositions.

3.2. SEM

Fig. 2(a-e) depicts the SEM morphologies of the NMNC-*x* samples. Further, magnified views of the samples with relatively smaller particle sizes is incorporated in order to resolve the particle morphology and estimate the average particle size. The representative elemental mapping of the NMNC-0.90 powder is depicted in Fig. S4(a-f). The agglomerated particles have a distorted hexagonal plate-like structure. An elucidation of the effect of Na^+ on the crystallization mechanism is beyond the scope of the present study. Still, it can be concluded that the distortion in the hexagonality of the particles is varied by varying the Na content. The average particle size of the NMNC-*x* samples increases significantly from 2.4 ± 0.5 μm to 10.3 ± 2.1 μm with an increase in *x* from 0.80 to 1.00. The increase in average particle size is expected to have a detrimental effect on the rate performance of the cathode at higher C rates due to the increase in the average Na^+ diffusion length through the solid cathode particles. The NMNC-0.90 sample with the P2/O3 phase ratio of ~ 0.85 has an average particle size of 5.1 ±

0.9 µm and a thickness of 1.0 ± 0.3 µm. In addition, elemental mapping of Na, Cu, Ni, Mn, and O in $Na_{0.90}Mn_{0.60}Ni_{0.30}Cu_{0.1}O_2$ particles using EDS elemental mapping shows a uniform distribution of these elements throughout the particles without any evident segregation (Fig. S4).

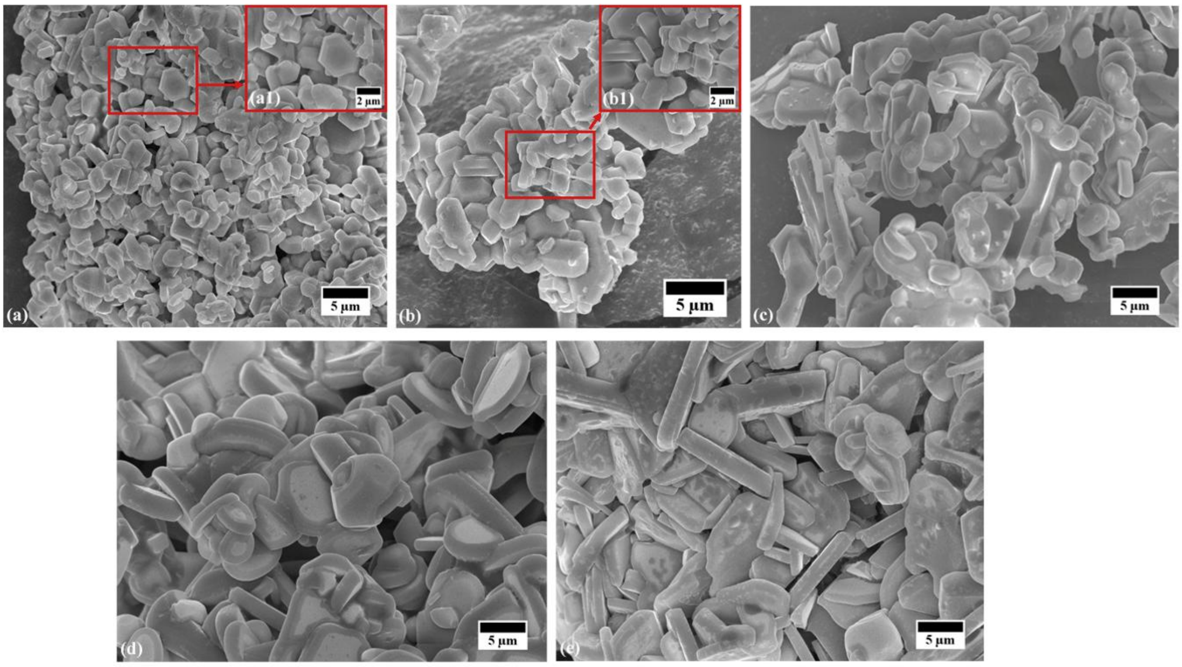

Fig. 2. SEM images of (a) NMNC-0.80 (inset a1 shows a higher magnification image), (b) NMNC-0.85 (higher magnification image is shown as inset b1), (c) NMNC-0.90, (d) NMNC-0.95, and (e) NMNC-1.00.

3.3. XPS

X-ray photoelectron spectroscopy (XPS) was employed to investigate the oxidation states of the transition metal ions in the NMNC-*x* cathode materials. Fig. 3 depicts the Mn 2p, Ni 2p, and Cu 2p spectra of the NMNC-*x* cathodes. Further the observed XPS data is depicted by open grey circles and the fitting curves are represented by the mustard colour lines in Fig. 3. Peaks due to Mn $2p_{3/2}$ and Mn $2p_{1/2}$ are visible in the Mn 2p XPS spectra (Fig. 3(a)) of NMNC-*x* cathodes. These can be deconvoluted into 4 peaks attributed to Mn^{4+} at ~643 and ~654 eV and

Mn^{3+} at ~642 and ~653 eV [54-56]. This suggests the coexistence of Mn^{4+} and Mn^{3+} in the NMNC-*x* cathode materials. The intensity of the peaks corresponding to Mn^{3+} increases continuously with Na content, indicating an increasing Mn^{3+}/Mn^{4+} ratio from 0 in NMNC-0.80 to 0.5 in NMNC-1.00. The Ni 2p spectrum (Fig. 3(b)) shows peaks that can be attributed to Ni $2p_{3/2}$ and Ni $2p_{1/2}$ at ~855 eV and ~872 eV, respectively, and their satellite peaks. This translates to a +2 oxidation state of Ni for all the samples [54-56]. Since the peak positions of the Ni $2p_{3/2}$ and Ni $2p_{1/2}$ are not altered with increasing *x* from 0.80 to 1.00, indicating that the oxidation state of Ni remains unchanged for all materials. Four characteristic peaks in the Cu 2p spectrum can be attributed to Cu $2p_{3/2}$ (~933 eV), Cu $2p_{1/2}$ (~953 eV), and their satellite peaks (Fig. 3(c)) [54-56]. Energies of the Cu $2p_{3/2}$ and Cu $2p_{1/2}$ peaks do not vary with varying *x* in NMNC-*x*, confirming a +2-oxidation state for Cu in all compositions.

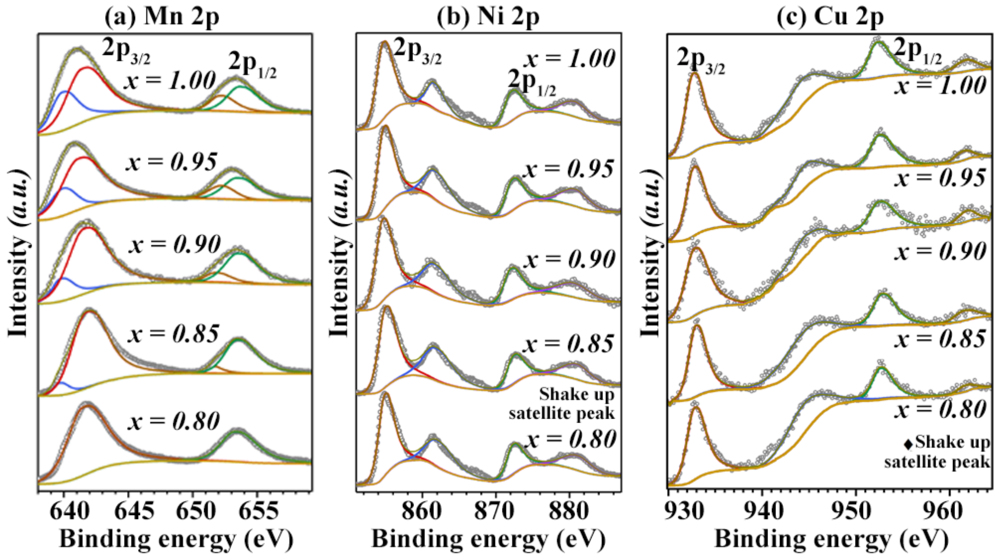

Fig. 3. (a) Mn 2p spectra, (b) Ni 2p spectra, and (c) Cu 2p spectra of NMNC-*x* samples ($0.80 \leq x \leq 1.00$)

Further, the XANES spectra of Mn and Ni taken at the K-edge of NMNC-0.80 and NMNC-1.00, along with the Mn_2O_3, MnO_2, and NiO spectra, are depicted in Fig. S5. The Mn K-edge spectrum of NMNC-1.00 is at a lower energy than that of NMNC-0.80, suggesting both Mn^{3+}

and Mn^{4+} in NMNC-1.00. The Ni K-edge spectra of both NMNC-0.80 and NMNC-1.00 coincide, indicating a similar oxidation state of Ni in both samples in compliance with the XPS results.

3.4. CV

The redox activity of NMNC-*x* electrodes with varying Na content was tested by cyclic voltammetry (CV) between 2.0 - 4.2 V at a scan rate of 0.1 mV s^{-1}. Fig. 4 illustrates the cyclic voltammograms of NMNC-0.80, NMNC-0.85, NMNC-0.90, NMNC-0.95, and NMNC-1.00, along with the major redox couples marked. The broad peaks at ~3.32/3.09 V and ~3.39/3.17 V indicate the Ni^{2+}/Ni^{4+} redox activity [49, 57, 58], and Cu^{2+}/Cu^{3+} redox reaction can be attributed to the peak at ~3.87/3.73 V [16, 28, 59] in the CV curve of NMNC-0.80 (Fig. 4(a)). The absence of redox peaks between the 2 V to 3 V in the 2nd & 3rd cycles indicates the inactivity of Mn^{4+} in the redox process. With increasing sodium content, the Ni^{2+}/Ni^{4+} redox peaks shift to 3.26/3.10 V and 3.43/3.25 V, while the Cu^{2+}/Cu^{3+} redox peaks shift to 3.91/3.75 V. A shift in the redox peak positions is due to the altered amounts of energy required for desodiation-sodiation in NNMC-*x* with different Na contents, despite the materials having the same ratio of transition metals. It is inferred that the local structure, determined by the initial Na concentration, vacancy, and Mn oxidation state, has a significant impact on the electrochemical processes.

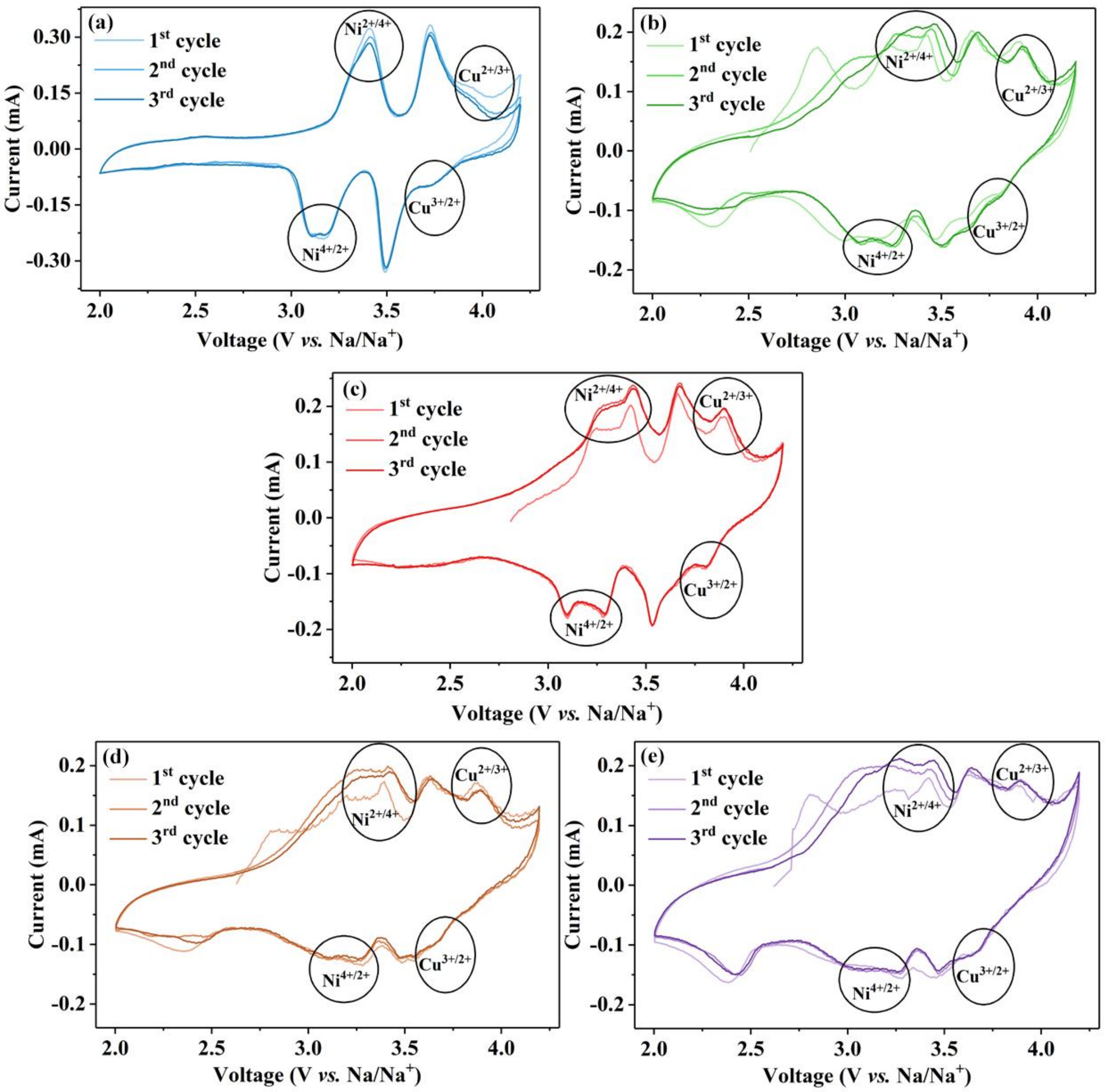

Fig. 4. Cyclic voltammograms of (a) NMNC-0.80, (b) NMNC-0.85, (c) NMNC-0.90, (d) NMNC-0.95, and (e) NMNC-1.00 samples at a scan rate of 0.1 mV s^{-1}.

In addition, new pairs of reversible peaks emerge at 2.80/2.44 V and 3.67/3.53 V, which can be assigned to Mn^{3+}/Mn^{4+} redox reaction [60, 61] and Na^+ vacancy ordering, respectively [51, 52, 62]. Further derivatives of the second cycle charge-discharge curves (dQ/dV) were calculated, and the corresponding dQ/dV vs. voltage (V) profiles of NMNC-*x* cathodes were plotted, as shown in Fig. S6. The Ni^{2+}/Ni^{4+} activity peaks between 3.0 V and 3.5 V, and the Cu^{2+}/Cu^{3+} redox peak at ~3.8/3.9 V can be observed for all samples. Furthermore, the NMNC-*x* cathodes with *x* ranging from 0.85 to 1.00 have a redox peak between 2.5-3.0 V, corresponding to Mn^{3+}/Mn^{4+} activity. An additional pair of peaks at ~3.61 V appears in the dQ/dV vs. V curves of NMNC-x ($0.85 \leq x \leq 1.00$), which indicates Na-ion vacancy ordering in accordance with the CV analysis.

3.5. GCD

To probe the effect of varying Na content on the specific capacity, rate performance, and cyclability of the NMNC-x cathodes were studied using the galvanostatic charge-discharge (GCD) tests at different current rates in the 2.0-4.2 V range. The GCD results are shown in Fig. 5. The 2.0-4.2 V range is selected because cycling at a lower voltage can lead to the degradation of the cathode material. In contrast, a higher cut-off voltage increases the likelihood of electrolyte degradation [63]. Fig. S7 depicts the first charge-discharge cycle of the NMNC-x cathodes. The initial coulombic efficiency improves with increasing Na content. This is due to the increasing O3 phase with a large Na^+ reservoir that balances the sodium deficient phase region, indicating that compounds with a higher O3 phase are suited for full cell realization. The theoretical specific capacities of NMNC-0.80, NMNC-0.85, NMNC-0.90, NMNC-0.95, and NMNC-1.00 are 174.84, 185.35, 195.63, 205.70, and 215.56 mAh g^{-1}, respectively. For these calculations, the amounts of Na-ion shuttling between positive and negative electrode are assumed to be 0.70 for NMNC-0.80 (0.3 $Ni^{2+/4+}$ & 0.1 $Cu^{2+/3+}$), 0.75 for NMNC-0.85 (0.3 $Ni^{2+/4+}$, 0.1 $Cu^{2+/3+}$, 0.05 $Mn^{3+/4+}$), 0.80 for NMNC-0.90 (0.3 $Ni^{2+/4+}$, 0.1 $Cu^{2+/3+}$, 0.10 $Mn^{3+/4+}$), 0.85 for NMNC-0.95 (0.3 $Ni^{2+/4+}$, 0.1 $Cu^{2+/3+}$, 0.15 $Mn^{3+/4+}$), and 0.90 for NMNC-1.00 (0.3 $Ni^{2+/4+}$, 0.1 $Cu^{2+/3+}$, 0.2 $Mn^{3+/4+}$). Fig. 5(a, b, c, d, and e) shows that the discharge capacity at 0.1C is 147.6, 151.2, 167.2, 175.8, and 187.6 mAh g^{-1} for NMNC-0.80, NMNC-0.85, NMNC-0.90, NMNC-0.95, and NMNC-1.00, respectively. The O3 dominant NMNC-1.00 shows higher specific discharge capacity compared to the P2 dominant NMNC-0.80 due to its higher Na content. At an increased 3C rate, the specific capacity decreases with increasing Na content. This is attributed to the increase in the average particle size and agglomeration of the particles with increasing Na, which hinders Na-ion extraction at high C rates. In addition, the lower diffusion coefficient of Na-ions in O3-type structures compared to that of the P2 type also contributes to the inferior rate performance at high C-rates. The two sets of plateaus result from Ni^{2+}/Ni^{4+} conversion above 3.0 V and Cu^{2+}/Cu^{3+} at 3.9 V. The charge-discharge profile of NMNC-0.90 has two plateaus above 3.5 V due to Na-ion vacancy ordering and Cu^{2+}/Cu^{3+} reaction.

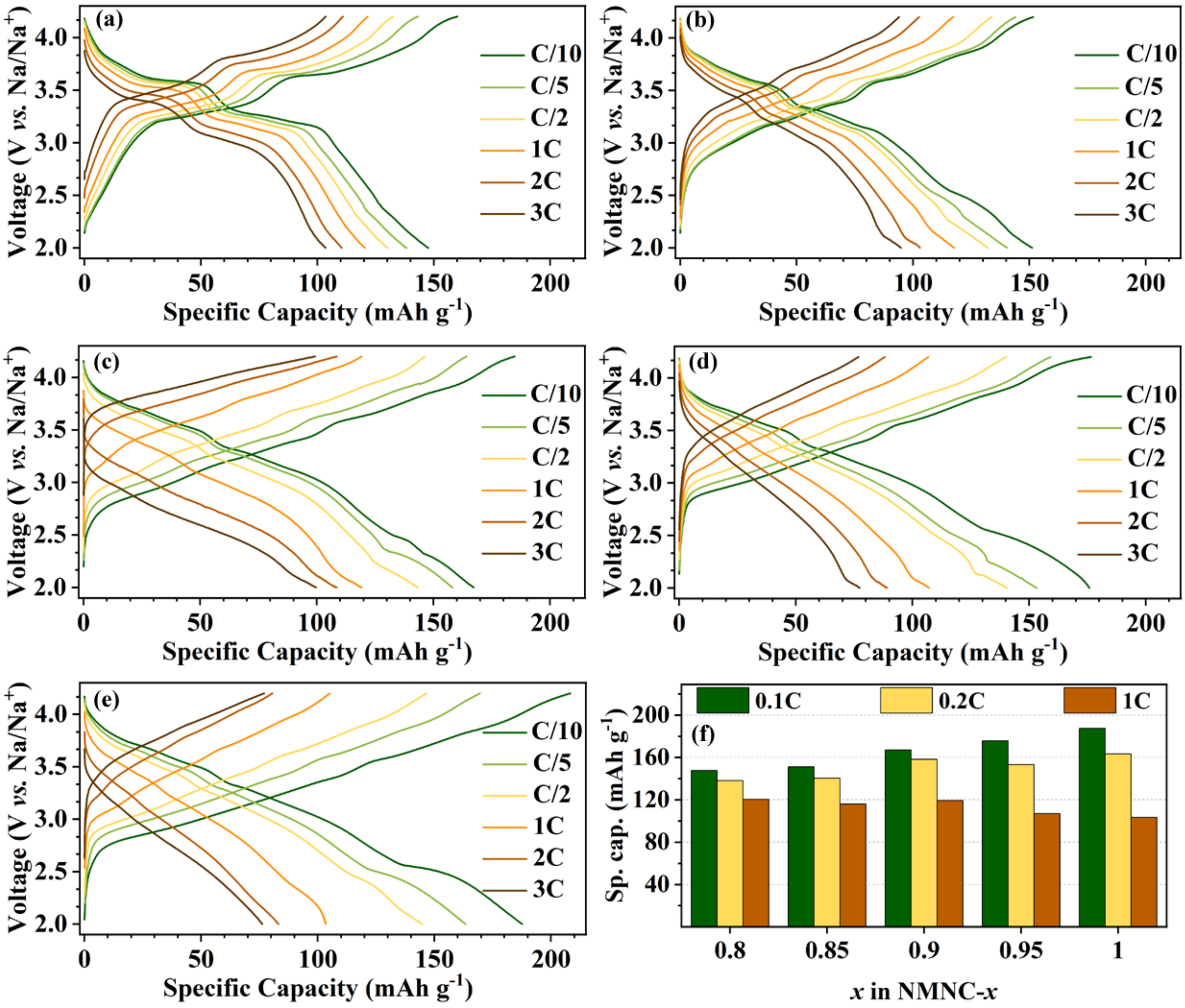

Fig. 5. Galvanostatic charge-discharge plots of (a) NMNC-0.80, (b) NMNC-0.85, (c) NMNC-0.90, (d) NMNC-0.95, (e) NMNC-1.00 at various C rates, and (f) comparison of specific capacities at different C rates.

The plateaus observed between 2.6 V and 2.0 V in the GCD profiles of NMNC-0.85, NMNC-0.90, NMNC-0.95, and NMNC-1.00 at low C-rates are due to Mn activation. Interestingly, the cathode with a P2/O3 ratio ~ 0.85 exhibits a higher polarisation when compared to cathodes with the dominant P2 (NMNC-0.8) or dominant O3 (NMNC-1.00) phase. This could be due to a larger strain produced during charge/discharge by the coexistence of the P2 and O3 phases. The voltage plateaus observed in the charge-discharge profiles are consistent with the CV and the dQ/dV vs. V curves. In addition, the energy efficiency of NMNC-*x* cathodes at 0.1C is depicted in Fig. S8. The shaded area under the curve represents the amount of energy recovered during the discharge against the total energy input during charging (area under the charging curve). The energy efficiency of NMNC-0.80, NMNC-0.85, NMNC-0.90, NMNC-0.95 and NMNC-1.00 is 92.1%, 88.7%, 89.8%, 86.8%, and 88.7%, respectively.

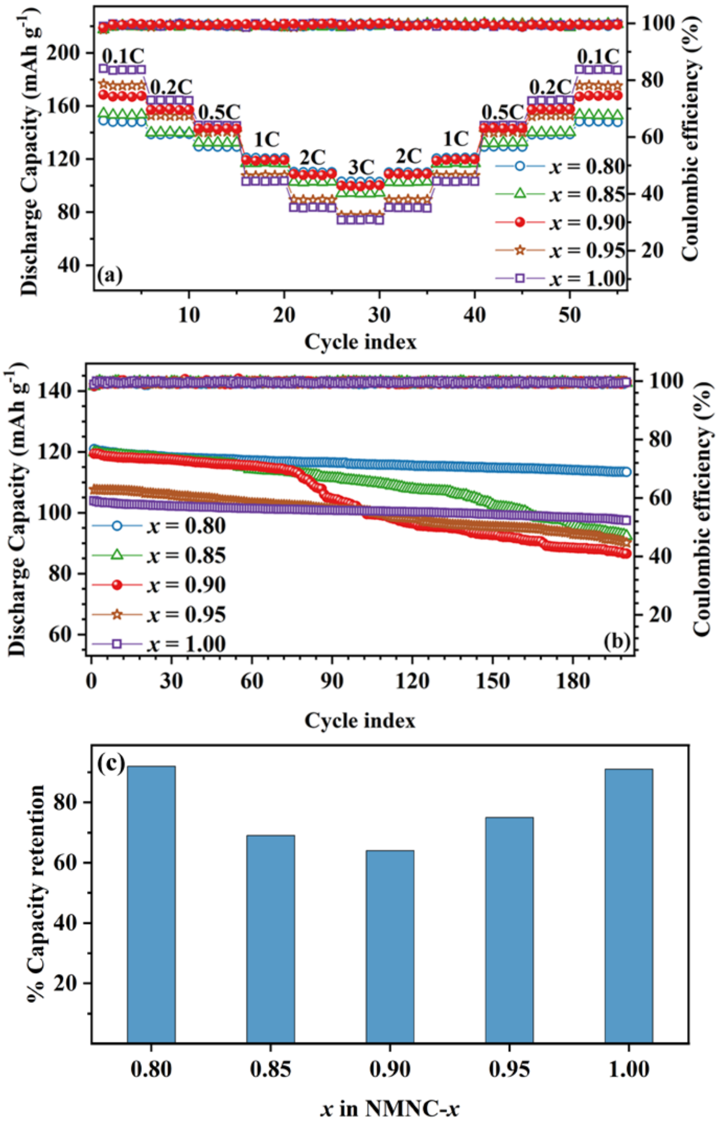

Fig. 6. (a) Discharge capacity and coulombic efficiency of the NMNC-*x* samples at various C-rates. (b) Cycle performance of NMNC-*x* at 1C for 200 cycles. (c) Comparison of % capacity retention after 200 cycles for NMNC-*x* cathodes.

Fig. 6(a) displays the rate capability of NMNC-*x* cathodes at various discharge currents corresponding to the 0.1 - 3C range. With an increased C-rate, the discharge capacity decreases for all cathodes. Upon decreasing the C-rate, all samples recover their initial discharge capacities. The NMNC-0.80 exhibits a discharge capacity of 103.5 mAh g^{-1} at 3C (~ 70 % of the specific capacity at 0.1C). This could be attributed to the +4 oxidation state of Mn in

NMNC-0.80, which induces Mn inactivity. In contrast, the NMNC-1.00 sample has a capacity of 187.8 mAh g^{-1} at 0.1C, which is reduced significantly to 76.3 mAh g^{-1} at 3C (~ 40% of the capacity at 0.1C). The NMNC-0.90 has a decent rate performance with a discharge capacity of 167 mAh g^{-1} at a lower 0.1C rate and a reduced capacity of 100 mAh g^{-1} (~ 60% of 167 mAh g^{-1}) at 3C. The substantial variation in the rate performances may be due to the varied local lattice environment in NMNC-*x* cathodes attributed to the different sodium contents in as-synthesized samples [64-66]. Na-ions occupy two sites in P2-type structures, with the face-shared triangular prism providing an open migration channel for Na^+. Therefore, the compounds with higher P2 phases have superior rate performance [67]. O3-type structures with one occupancy site for Na^+ share six edges with TMO_6 octahedrons. Here, the Na-ions migrate through the smaller tetrahedra, which restricts the movement of ions, lowering the ionic conductivity and the rate performance of compounds with higher O3 phase fraction [68]. Given the excellent rate performance and cyclability, the NMNC-0.80 cathode could be used for grid storage related applications. Similarly, the NMNC-1.00 sample is attractive for application as a cathode in batteries for portable electronic devices due to its excellent cyclability and good specific capacity.

To investigate the effect of varying sodium content on the cycling stability, the NMNC-*x* cathode materials were tested at 1C between 2.0-4.2 V, and the results are displayed in Fig. 6(b). After 200 cycles, the capacity retention of NMNC-0.80, NMNC-0.85, NMNC-0.90, NMNC-0.95, and NMNC-1.00 is 92%, 69%, 64%, 75%, and 91%, respectively, with a coulombic efficiency of over 99%. The cyclability data indicates that the cathodes with dominant P2 or O3 phase retain higher capacity than the high-rate performing NMNC-0.90. The extensively studied synergistic effect in biphasic layered oxides contributes to the high cyclability of NMNC-0.80 and NMNC-1.00. In contrast, the NMNC-0.90 shows poor cyclability, with only 64% capacity retention after 200 cycles. Table S9 compares the reported specific capacity and cyclability of various biphasic cathodes for sodium-ion batteries. Therefore, it is inferred from these results that the introduction of a minor P2 or O3 phase allows better cyclability. The changes in lattice parameters during GCD and their impact on cyclability are discussed in the *operando* SXRD section.

3.6. GITT

The galvanostatic intermittent titration technique (GITT) was employed to investigate the Na-ion diffusion kinetics in NMNC-*x* cathode materials during charge-discharge (Figs. 7 & S9). This technique involves subjecting the cell to a galvanostatic process for a specified period, followed by a resting time. In the present investigation, the cells were cycled twice before GITT measurements by successively applying a constant current pulse equivalent to 0.1C for 10 minutes, then relaxing the cell for 30 minutes to achieve pseudo-equilibrium. Eq. 2 is used to determine the diffusion coefficient of Na-ions in the cathode materials, assuming that the process adheres to Fick's first law [69].

$$D_{Na^+} = \frac{4}{\pi\tau}\left(\frac{m_B V_m}{M_B S}\right)^2 \left(\frac{\Delta E_S}{\Delta E_\tau}\right)^2 \qquad (t \ll L^2 \,/\, D) \qquad (2)$$

Here, τ is the duration of a single pulse of constant current, m_B is the mass of active material, V_m & M_B are the molar volume & molar mass of cathode material, and S is the electrode's surface area. ΔE_S and ΔE_τ represent the voltage change during the constant current pulse and the steady-state voltage change, respectively.

Fig. 7(d) shows a single GITT titration unit displaying all the elements discussed above. Sodium-ion diffusion coefficient (D_{Na}^+) values of NMNC-0.80, NMNC-0.90, and NMN-1.00 are distributed between 1.35×10^{-11} – 2.72×10^{-10} cm^2 s^{-1}, 1.84×10^{-12} – 1.56×10^{-10} cm^2 s^{-1}, and 1.27×10^{-12} – 2.20×10^{-10} cm^2 s^{-1}, respectively. The D_{Na}^+ of NMNC-0.85 and NMNC-0.95 are in the range of 2.43×10^{-12} – 2.39×10^{-10} cm^2 s^{-1} and 7.63×10^{-13} – 1.60×10^{-10} cm^2 s^{-1}

respectively. Comparing the D_{Na}^+, the cathodes with either dominant P2 or O3 phases have a slightly higher diffusion coefficient than that with equal phase fractions of P2 and O3. This could be attributed to the lower values of strain generated during discharging for the NMNC-0.80 and NMNC-1.00.

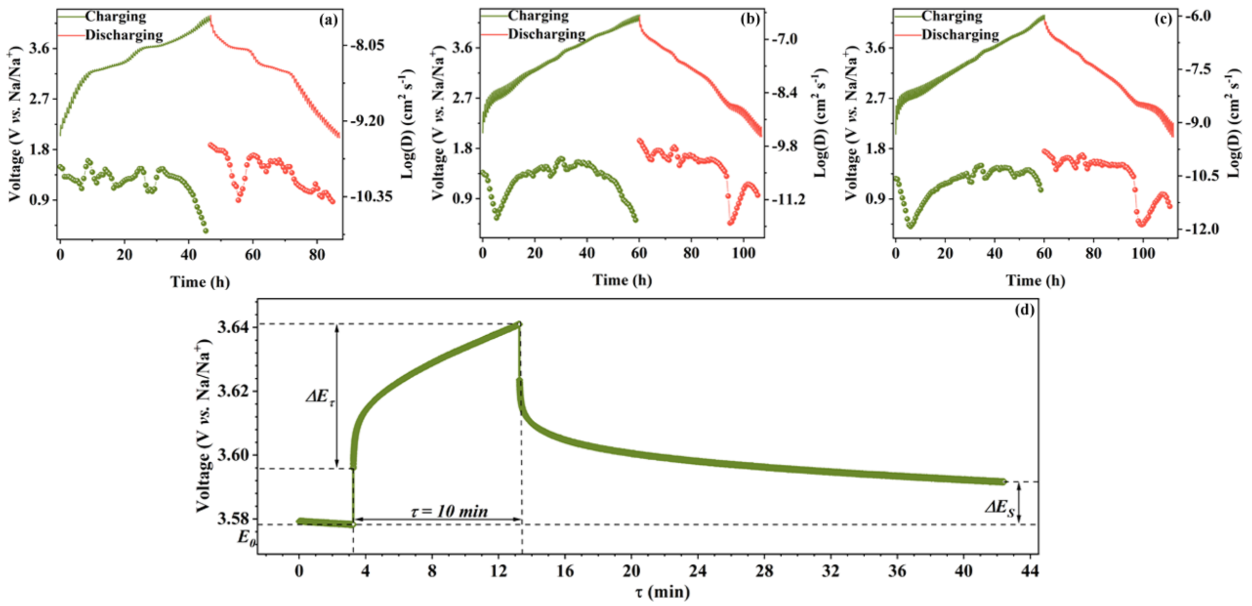

Fig. 7. GITT profile of (a) NMNC-0.80, (b) NMNC-0.90, and (c) NMNC-1.00 cathodes along with diffusion coefficient of Na^+ at different stages during charge-discharge. (d) A single titration unit in GITT.

Fig. 7(a-c) reveals that the diffusion coefficient value decreases at higher voltages when the structure contains fewer Na^+ cations, indicating that the electrochemical process is relatively slow in such voltages [70]. Similarly, when discharging to lower voltages, the diffusion coefficient declines rapidly when the cathode becomes saturated with sodium ions, indicating inferior diffusion kinetics. Even at 4.2 V, the values of D_{Na}^+ of the NMNC-0.80 and NMNC-1.00 (1.35×10^{-11} & 1.27×10^{-12} cm^2 s^{-1}) are still slightly higher than that of NMNC-0.90 (1.84×10^{-12}).

3.7. *Operando* Synchrotron XRD

Operando Synchrotron XRD measurements were performed to understand the structural transformation in NMNC-x (x = 0.80, 0.90, and 1.00) during charging-discharging at 0.1C. Fig. 8 shows the *operando* Synchrotron XRD pattern of the NMNC-0.90 sample at different charge states between 2.0 and 4.2 V, while that of NMNC-0.80 and NMNC-1.00 is displayed in Fig. S10 & S11, respectively. During charging from OCV, the (003) peak of the O3 phase shifts towards lower angles, and eventually, the O3 fully transforms to the P3 phase at ~ 3.4 V. On further charging, the (006) diffraction peaks of the P3 phase continue to shift towards a lower angle, which is due to the slipping of the TMO_2 layers to reduce the electrostatic repulsive force (Fig. 8(a1)). P2 (100) diffraction peak at $2\theta \approx 19.2°$ and O3 (101) & P3 (101) diffraction peak at $2\theta \approx 19.4°$ also shift towards higher angles, indicating a decrease in lattice parameter a of all phases (Fig. 8(a2)). On the other hand, the position of the P2 (002) diffraction peaks shift marginally towards lower angles during the charging process, suggesting only a slight increase in the c-lattice parameter (Fig. 8(a1)). During discharging, the (00l) diffraction peaks corresponding to the O3 phase emerge gradually, indicating the transformation of the P3 phase back to the O3 phase. The (100) and (102) diffraction peaks of the P2 phase also return to their original position, and no new diffraction peaks appear at the end of the discharge process, implying the reversibility of structural changes that occurred during charging/discharging.

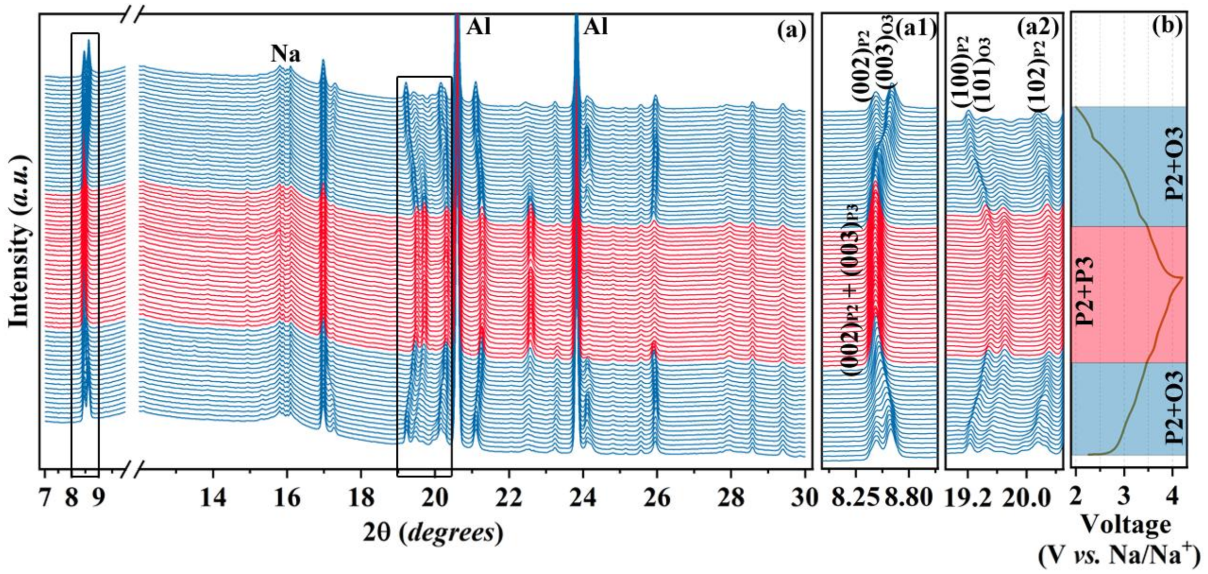

Fig. 8. (a) *Operando* Synchrotron XRD pattern of NMNC-0.90 sample at different charge states between 4.2 and 2.0 V during charging and discharging at 0.1C. Enlarged view of (a1) (002) peak of P2 and (003) peak of O3 showing phase transformation of O3 to P3 and change in the *c*-lattice parameter. (a2) (100) & (102) peak of P2 and (101) peak of O3 showing the change in the *a*-lattice parameter. (b) Corresponding GCD curve showing various states of charge and discharge.

To quantify the variations in the lattice parameters of NMNC-*x* during charging/discharging, LeBail refinement of *operando* Synchrotron XRD data at different voltages was performed. The fitted patterns, difference curves, Bragg positions, and variation of *a* and *c* lattice parameters during charging/discharging are given in Fig. 9 and Figs. S12 & S13. For NMNC-0.80 & 1.00 (with dominant P2 and O3 phases, respectively), the change in the *c* parameter ($\Delta c = \frac{c_{4.2V}-c_{2.0V}}{c_{4.2V}} \times 100\%$) of the P2 phase remains negligible (~ –0.06%) during discharge from 4.2 V to 2.0 V for both samples; however, the corresponding value of Δ*c* for the O3 phase is ~ –1.57%. The value of change in lattice parameter *a* (Δ*a*) during discharge is ~ +0.96% for P2 in NMNC-0.80 and +0.89 % for the O3 phase in NMNC-1.00. As the P2/O3 phase ratio increases to ~ 0.85 for NMNC-0.90, the Δ*c* during discharge increases to – 0.16% for the P2 phase and approximately – 1.85% for the O3 phase, which is relatively higher compared to NMNC-0.80 and NMNC-1.00. The value of change in lattice parameter *a* (Δ*a*) during discharge is ~ +1.15% and ~ +1.02% for the P2 and O3 phases, respectively. This increase in the value of Δ*c* suggests that when the P2 and O3 phases are present in similar proportions, there is a significant mismatch in the levels of the strain developed in the P2 and O3 phases in NMNC-0.90 particles during charge/discharge cycles. This mismatch in strain within the particle ultimately damages the cathode during cycling, leading to inferior performance in terms of capacity retention. In contrast, the introduction of a minor O3 phase in a P2-dominant phase (as in NMNC-0.80) or vice versa (NMNC-1.00) resulted in an overall lesser mismatch of strain during sodium extraction and insertion simply because these samples are dominated by either phase. This allows the cathode to maintain its structural integrity and explains the superior capacity retention of the NMNC-0.80 and NMNC-1.00 samples.

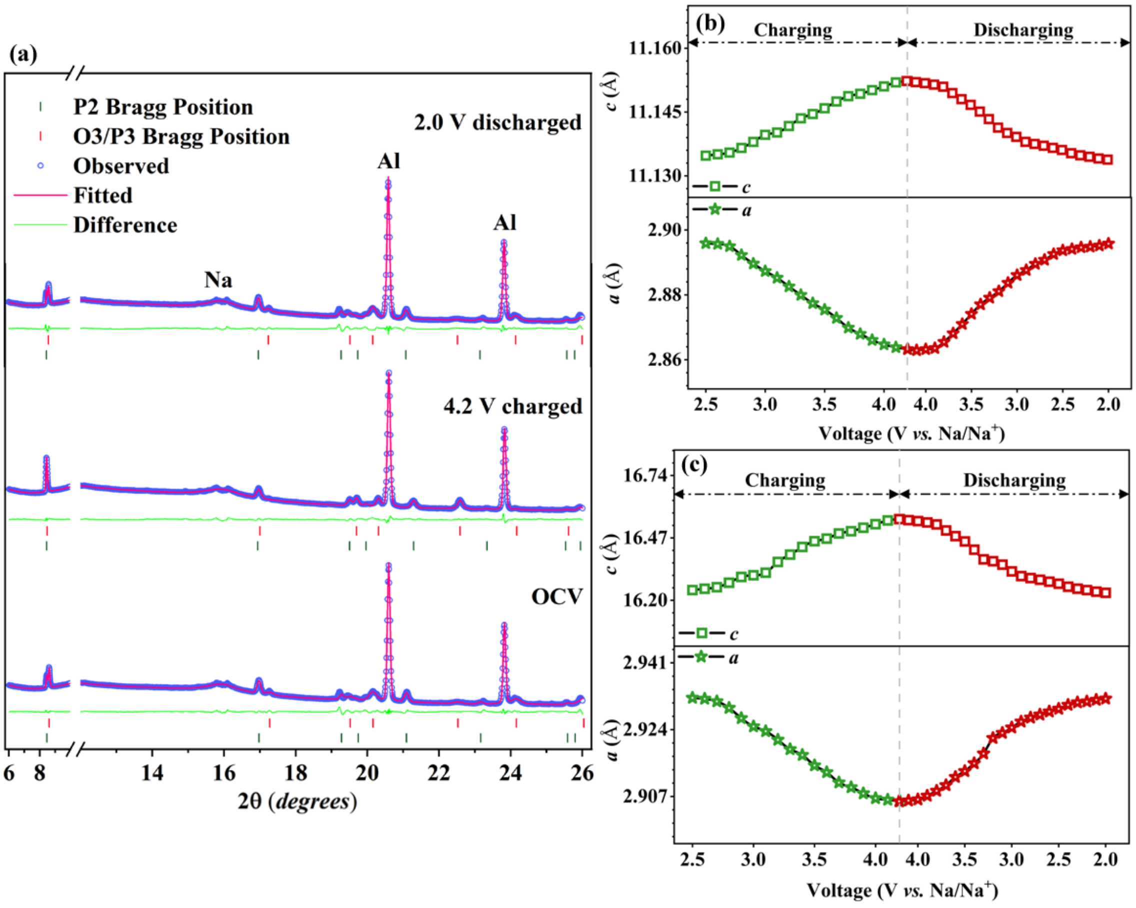

Fig. 9. (a) LeBail fitted operando Synchrotron XRD data profiles at OCV ~ 2.5 V, 4.2 V, and 2.0 V for NMNC-0.90. Variation in lattice parameters of (b) P2 phase and (c) O3 phase during charging/ discharging.

3.8. Ex-situ XPS

Ex-situ XPS studies were performed on the NMNC-0.80 and NMNC-1.00 cathodes at fully charged and discharged states, and the results are depicted in Figs. S14 & S15. The Mn 2p spectra of NMNC-0.80 and NMNC-1.00 showed that Mn maintained a 4+ oxidation state throughout the charge/discharge process in the former, while Mn^{3+} oxidized to Mn^{4+} during charging in the latter (Fig. S14). After discharging to 2.0 V, Mn^{4+} reduces partially back to Mn^{3+} [55, 71]. The analysis of Ni 2p spectra shows that when charged to 4.2 V, the Ni 2p peaks shift slightly to a higher value of binding energy, indicating oxidation of Ni^{2+} to Ni^{4+} during charging in both NMNC-0.80 and NMNC-1.00 [55]. When discharged to 2.0 V, all the peaks return to their original states. This validates the reversibility of all redox reactions, thereby affirming the structural stability of NMNC-0.80 and NMNC-1.00 during cycling.

3.9. Full cell performance

The electrochemical behaviour of a full cell fabricated with $Na_{1.00}Mn_{0.60}Ni_{0.30}Cu_{0.10}O_2$ as the cathode and hard carbon (HC) as the anode is depicted in Fig. 10(c). The hard carbon anode was sodiated and de-sodiated in a half-cell configuration using Na metal as the counter electrode. The sodiated HC was collected after de-crimping the coin-cell, and was then used in the full cell. The specific capacity of the hard carbon obtained in 2nd cycle was ~ 275 mAh g^{-1} (Fig. 10(a)). The full cell exhibited a capacity of ~ 108 mAh g^{-1} (where, mass is of cathode & anode active materials only) with a nominal voltage of ~ 3.4 V at 0.1C when cycled in the 1.75 V - 4.0 V range. The full cell showed a capacity retention of ~ 80% after 50 cycles. The cycling performance exhibited by the full cell is poor compared to that of the cathode in half cell and could be enhanced by balancing the active material mass loadings and stabilizing the solid electrolyte interphase (SEI) layer through appropriate additives in the electrolyte.

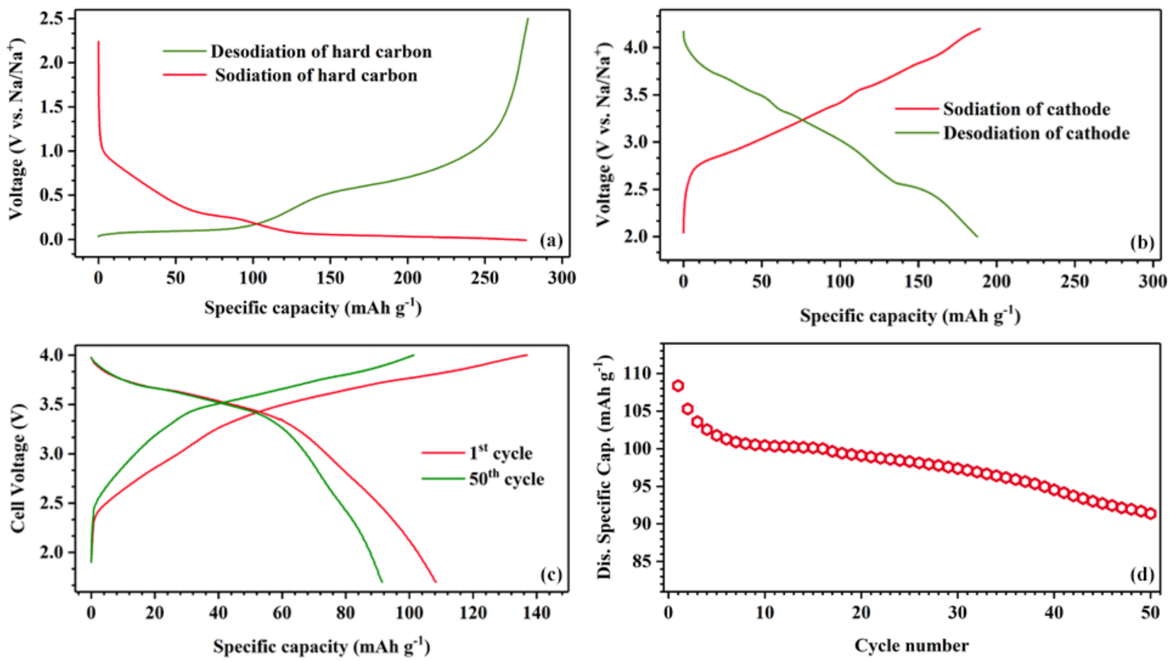

Fig. 10. The GCD curves of (a) hard carbon *vs.* Na metal, (b) $Na_{1.00}Mn_{0.60}Ni_{0.30}Cu_{0.10}O_2$ *vs.* Na metal. (c) The 1st and 50th cycle GCD curves of full cell with NMNC-1.00 cathode and HC anode at 0.1C. (d) Cycle performance of NMNC-1.00||HC full cell at 0.1C for 50 cycles.

Conclusions

In summary, biphasic P2/O3 $Na_xMn_{0.60}Ni_{0.30}Cu_{0.10}O_2$ ($0.80 \leq x \leq 1.00$) series of cathode materials with varying P2 and O3 phase fractions were synthesized by tuning the Na content to investigate the effect of phase fraction on electrochemical performance. The coexistence of P2 and O3 phases has been verified by the XRD patterns. Further, a *peak intensity ratio* method is introduced to obtain an approximate value of the phase fractions, and the results match very well with the quantitative Rietveld refinement of the XRD data. The O3 phase fraction increases from 13% to 89% with an increase in Na content from 0.80 to 1.00. Interestingly, there is a negligible change in the lattice parameter *c* of the P2 phases during discharge (~

0.06%) for all samples. On the contrary, the change in the lattice parameter *c* of the O3 phase increases from ~ 1.57% for NMNC-0.80 & 1.00 to ~ 1.85% for NMNC-0.90. Consequently, the capacity retention at 1C for NMNC-0.90 is only 64% after 200 cycles, although it has a higher rate capability (a reversible capacity of 100 mAh g^{-1} at 3C). This study establishes that the presence of P2 & O3 phases in nearly equal amounts in the biphasic structures (NMNC-0.90) is unable to alleviate the strain caused by the sodium extraction and insertion, resulting in the damaged structure. The presence of a minor O3 phase in a P2 dominant material (NMNC-0.80) or vice-versa (NMNC-1.00), on the other hand, limits the mismatch in levels of strain during charging/discharging and stabilizes the structure. The NMNC-0.80 cathode material exhibited superior rate capability (a reversible capacity of 103 mAh g^{-1} at 3C) and better cyclic stability (92% capacity retention after 200 cycles at 1C). The NMNC-1.00 cathode shows a high specific capacity (188 mAh g^{-1} at 0.1C) and 91% capacity retention after 200 cycles at 1C. The full cell (NMNC-1.00 as cathode and hard carbon as the anode) exhibited a capacity of ~ 108 mAh g^{-1} with a nominal voltage of ~ 3.4 V at 0.1C. These results signify the role of phase fractions in controlling the lattice mismatch in biphasic structures and provide a novel perspective on tuning the phase fraction for high-performing cathodes for Na-ion batteries.

Author contributions

Samriddhi Saxena: Designed the research, material synthesis, fabrication and electrochemical characterization of half-cells, formal analysis, and writing the original draft; **Manish Badole:** SEM measurements, Writing – review & editing; **Hari Narayanan Vasavan:** XRD measurements, Writing – review & editing; **Velaga Srihari:** Supervised *operando* Synchrotron XRD data collection and analysis; **Asish Kumar Das:** Writing – review & editing; **Pratiksha Gami:** Writing – review & editing; **Sonia Deswal:** performed XPS measurements; **Pradeep Kumar:** XPS analysis; **Sunil Kumar:** Funding acquisition, conceptualization, supervision, conceived the idea and supervised the work; wrote the manuscript with input from all authors

Conflicts of interest

There are no conflicts of interest to declare.

Acknowledgments

SS thanks the Ministry of Education, Government of India for the Prime Minister's Research Fellowship (Application number: 2103359). SK thanks the Science and Engineering Research Board (SERB), Govt. of India, for the financial support (grant number: CRG/2021/005548). The authors acknowledge DST and SAIF/CRNTS, IIT Bombay, for providing the ICP-AES analytical facility and Dr. S. N. Jha for his help in recording the EXAFS spectra at RRCAT, Indore, India.

References

[1] N. Yabuuchi, K. Kubota, M. Dahbi, S. Komaba, Research development on sodium-ion batteries, Chemical Reviews 114(23) (2014) 11636-11682. https://doi.org/https://doi.org/10.1021/cr500192f.

[2] M. Armand, J.M. Tarascon, Building better batteries, Nature 451(7179) (2008) 652-657. https://doi.org/10.1038/451652a.

[3] H.N. Vasavan, M. Badole, S. Dwivedi, S. Kumar, Structural and transport properties of P2-Type $Na_{0.70}Ni_{0.20}Cu_{0.15}Mn_{0.65}O_2$ layered oxide, Ceramics International 48(19, Part B) (2022) 28986-28993. https://doi.org/https://doi.org/10.1016/j.ceramint.2022.04.206.

[4] H. Chen, X. Yang, P. Lv, P. Tian, S. Wan, Q. Liu, Mn-doped FeS with larger lattice spacing as advance anode for sodium ion half/full battery, Chemical Engineering Journal 450 (2022) 137960. https://doi.org/https://doi.org/10.1016/j.cej.2022.137960.

[5] S. Cao, X. Xu, Q. Liu, H. Chen, H. Zhu, Y. Lin, Co quantum dots embedded in modified montmorillonite loaded with graphitized carbon as an ultra-stable anode material for sodium-ion battery, Journal of Colloid and Interface Science 650 (2023) 1073-1085. https://doi.org/https://doi.org/10.1016/j.jcis.2023.07.064.

[6] H. Chen, P. Lv, P. Tian, S. Cao, S. Yuan, Q. Liu, Hollow sphere of heterojunction (NiCu)S/NC as advanced anode for sodium-ion battery, Journal of Energy Chemistry 82 (2023) 248-258. https://doi.org/https://doi.org/10.1016/j.jechem.2023.03.018.

[7] M. Chen, Q. Liu, S.W. Wang, E. Wang, X. Guo, S.L. Chou, High-abundance and low-cost metal-based cathode materials for sodium-ion batteries: problems, progress, and key technologies, Advanced Energy Materials 9(14) (2019) 1803609. https://doi.org/ https://doi.org/10.1002/aenm.201803609.

[8] V. Palomares, P. Serras, I. Villaluenga, K.B. Hueso, J. Carretero-González, T. Rojo, Na-ion batteries, recent advances and present challenges to become low cost energy storage systems, Energy & Environmental Science 5(3) (2012) 5884-5901. https://doi.org/10.1039/C2EE02781J.

[9] Y. Niu, Y. Zhao, M. Xu, Manganese-based polyanionic cathodes for sodium-ion batteries, Carbon Neutralization 2(2) (2023) 150-168. https://doi.org/https://doi.org/10.1002/cnl2.48.

[10] Q. Liu, Z. Hu, M. Chen, C. Zou, H. Jin, S. Wang, S.L. Chou, S.X. Dou, Recent progress of layered transition metal oxide cathodes for sodium-ion batteries, Small 15(32) (2019) 1805381. https://doi.org/https://doi.org/10.1002/smll.201805381.

[11] V. Palomares, M. Casas-Cabanas, E. Castillo-Martínez, M.H. Han, T. Rojo, Update on Na-based battery materials. A growing research path, Energy & Environmental Science 6(8) (2013) 2312-2337. https://doi.org/10.1039/C3EE41031E.

[12] M.H. Han, E. Gonzalo, G. Singh, T. Rojo, A comprehensive review of sodium layered oxides: powerful cathodes for Na-ion batteries, Energy & Environmental Science 8(1) (2015) 81-102. https://doi.org/10.1039/C4EE03192J.

[13] C. Delmas, C. Fouassier, P. Hagenmuller, Structural classification and properties of the layered oxides, Physica B+ c 99(1-4) (1980) 81-85. https://doi.org/https://doi.org/10.1016/0378-4363(80)90214-4.

[14] H.N. Vasavan, M. Badole, S. Saxena, A.K. Das, S. Deswal, P. Kumar, S. Kumar, Excellent Structural Stability-Driven Cyclability in P2-Type Ti-Based Cathode for Na-Ion Batteries, ACS Applied Energy Materials 6(4) (2023) 2440-2447. https://doi.org/https://doi.org/10.1021/acsaem.2c03750.

[15] H.N. Vasavan, M. Badole, S. Dwivedi, D. Kumar, P. Kumar, S. Kumar, Enhanced rate performance and specific capacity in Ti-substituted P2-type layered oxide enabled by crystal structure and particle morphology modifications, Chemical Engineering Journal 448 (2022) 137662. https://doi.org/https://doi.org/10.1016/j.cej.2022.137662.

[16] Y. Li, Z. Yang, S. Xu, L. Mu, L. Gu, Y.-S. Hu, H. Li, L. Chen, Air-Stable Copper-Based P2-$Na_{7/9}Cu_{2/9}Fe_{1/9}Mn_{2/3}O_2$ as a New Positive Electrode Material for Sodium-Ion Batteries, Advanced Science 2(6) (2015) 1500031. https://doi.org/https://doi.org/10.1002/advs.201500031.

[17] L. Yang, S.-h. Luo, Y. Wang, Y. Zhan, Q. Wang, Y. Zhang, X. Liu, W. Mu, F. Teng, Cu-doped layered P2-type $Na_{0.67}Ni_{0.33-x}Cu_xMn_{0.67}O_2$ cathode electrode material with enhanced electrochemical performance for sodium-ion batteries, Chemical Engineering Journal 404 (2021) 126578. https://doi.org/10.1016/j.cej.2020.126578.

[18] Y. Zhang, R. Zhang, Y. Huang, Air-Stable Na_xTMO_2 Cathodes for Sodium Storage, Frontiers in Chemistry 7 (2019). https://doi.org/10.3389/fchem.2019.00335.

[19] K. Wang, Z.-G. Wu, G. Melinte, Z.-G. Yang, A. Sarkar, W. Hua, X. Mu, Z.-W. Yin, J.-T. Li, X.-D. Guo, B.-H. Zhong, C. Kübel, Preparation of intergrown P/O-type biphasic layered oxides as high-performance cathodes for sodium ion batteries, Journal of Materials Chemistry A 9(22) (2021) 13151-13160. https://doi.org/10.1039/D1TA00627D.

[20] Z. Lu, J.R. Dahn, In Situ X-Ray Diffraction Study of $P2-Na_{2/3}[Ni_{1/3}Mn_{2/3}]O_2$, Journal of the Electrochemical Society 148(11) (2001) A1225. https://doi.org/10.1149/1.1407247.

[21] S. Komaba, N. Yabuuchi, T. Nakayama, A. Ogata, T. Ishikawa, I. Nakai, Study on the Reversible Electrode Reaction of $Na_{1-x}Ni_{0.5}Mn_{0.5}O_2$ for a Rechargeable Sodium-Ion Battery, Inorganic Chemistry 51(11) (2012) 6211-6220. https://doi.org/10.1021/ic300357d.

[22] S. Jamil, Y. Feng, M. Fasehullah, G. Ali, B. Wu, Y.-J. Guo, B. Jabar, A. Mansoor, Y.-B. Niu, M. Xu, Stabilizing anionic redox in Mn-rich P2-type layered oxide material by Mg substitution, Chemical Engineering Journal 471 (2023) 144450. https://doi.org/https://doi.org/10.1016/j.cej.2023.144450.

[23] B. Peng, Z. Sun, L. Zhao, J. Li, G. Zhang, Dual-Manipulation on P2-$Na_{0.67}Ni_{0.33}Mn_{0.67}O_2$ Layered Cathode toward Sodium-Ion Full Cell with Record Operating Voltage Beyond 3.5 V, Energy Storage Materials 35 (2021) 620-629. https://doi.org/10.1016/j.ensm.2020.11.037.

[24] L. Yang, L.-Y. Kuo, J.M. López del Amo, P.K. Nayak, K.A. Mazzio, S. Maletti, D. Mikhailova, L. Giebeler, P. Kaghazchi, T. Rojo, P. Adelhelm, Structural Aspects of P2-Type $Na_{0.67}Mn_{0.6}Ni_{0.2}Li_{0.2}O_2$ (MNL) Stabilization by Lithium Defects as a Cathode Material for Sodium-Ion Batteries, Advanced Functional Materials 31(38) (2021) 2102939. https://doi.org/10.1002/adfm.202102939.

[25] Y. Xie, E. Gabriel, L. Fan, I. Hwang, X. Li, H. Zhu, Y. Ren, C. Sun, J. Pipkin, M. Dustin, M. Li, Z. Chen, E. Lee, H. Xiong, Role of Lithium Doping in P2-$Na_{0.67}Ni_{0.33}Mn_{0.67}O_2$ for Sodium-Ion Batteries, Chemistry of Materials 33(12) (2021) 4445-4455. https://doi.org/10.1021/acs.chemmater.1c00569.

[26] X. Wu, G.-L. Xu, G. Zhong, Z. Gong, M.J. McDonald, S. Zheng, R. Fu, Z. Chen, K. Amine, Y. Yang, Insights into the Effects of Zinc Doping on Structural Phase Transition of P2-Type Sodium Nickel Manganese Oxide Cathodes for High-Energy Sodium Ion Batteries, ACS Applied Materials & Interfaces 8(34) (2016) 22227-22237. https://doi.org/10.1021/acsami.6b06701.

[27] X. Wu, J. Guo, D. Wang, G. Zhong, M.J. McDonald, Y. Yang, P2-type $Na_{0.66}Ni_{0.33-x}Zn_xMn_{0.67}O_2$ as new high-voltage cathode materials for sodium-ion batteries, Journal of Power Sources 281 (2015) 18-26. https://doi.org/10.1016/j.jpowsour.2014.12.083.

[28] L. Wang, Y.-G. Sun, L.-L. Hu, J.-Y. Piao, J. Guo, A. Manthiram, J. Ma, A.-M. Cao, Copper-substituted $Na_{0.67}Ni_{0.3-x}Cu_xMn_{0.7}O_2$ cathode materials for sodium-ion batteries with suppressed P2–O2 phase transition, Journal of Materials Chemistry A 5(18) (2017) 8752-8761. https://doi.org/10.1039/C7TA00880E.

[29] T. Chen, W. Liu, F. Liu, Y. Luo, Y. Zhuo, H. Hu, J. Guo, J. Yan, K. Liu, Benefits of Copper and Magnesium Cosubstitution in $Na_{0.5}Mn_{0.6}Ni_{0.4}O_2$ as a Superior Cathode for Sodium Ion Batteries, ACS Applied Energy Materials 2(1) (2019) 844-851. https://doi.org/10.1021/acsaem.8b01909.

[30] M. Yan, K. Xu, Y.-X. Chang, Z.-Y. Xie, S. Xu, Cu/Ti co-doping boosting P2-type Fe/Mn-based layered oxide cathodes for high-performance sodium storage, Journal of Colloid and Interface Science 651 (2023) 696-704. https://doi.org/https://doi.org/10.1016/j.jcis.2023.07.195.

[31] S. Zheng, G. Zhong, M.J. McDonald, Z. Gong, R. Liu, W. Wen, C. Yang, Y. Yang, Exploring the working mechanism of Li^+ in O3-type $NaLi_{0.1}Ni_{0.35}Mn_{0.55}O_2$ cathode materials for rechargeable Na-ion batteries, Journal of Materials Chemistry A 4(23) (2016) 9054-9062. https://doi.org/10.1039/C6TA02230H.

[32] L. Yu, Y.-X. Chang, M. Liu, Y.-H. Feng, D. Si, X. Zhu, X.-Z. Wang, P.-F. Wang, S. Xu, O3-Type $Na_{0.95}Ni_{0.40}Fe_{0.15}Mn_{0.3}Ti_{0.15}O_2$ Cathode Materials with Enhanced Storage Stability for High-Energy Na-Ion Batteries, ACS Applied Materials & Interfaces 15(19) (2023) 23236-23245. https://doi.org/10.1021/acsami.3c02514.

[33] J.E. Wang, H. Kim, Y.H. Jung, D.K. Kim, D.J. Kim, Designing High Energy Sodium-Ion Battery Cathodes by Utilizing P2/O3 Biphasic Structure and Lithium Honeycomb Ordering, Small 17(30) (2021) 2100146.

[34] Z. Liu, C. Zhou, J. Liu, L. Yang, J. Liu, M. Zhu, Phase tuning of P2/O3-type layered oxide cathode for sodium ion batteries via a simple Li/F co-doping route, Chemical Engineering Journal 431 (2022) 134273. https://doi.org/10.1016/j.cej.2021.134273.

[35] S. Saxena, H.N. Vasavan, M. Badole, A.K. Das, S. Deswal, P. Kumar, S. Kumar, Tailored P2/O3 phase-dependent electrochemical behavior of Mn-based cathode for sodium-ion batteries, Journal of Energy Storage 64 (2023) 107242. https://doi.org/https://doi.org/10.1016/j.est.2023.107242.

[36] B. Xiao, X. Liu, M. Song, X. Yang, F. Omenya, S. Feng, V. Sprenkle, K. Amine, G. Xu, X. Li, D. Reed, A general strategy for batch development of high-performance and cost-effective sodium layered cathodes, Nano Energy 89 (2021) 106371. https://doi.org/https://doi.org/10.1016/j.nanoen.2021.106371.

[37] J. Liu, J. Zhou, Z. Zhao, Z. Che, J. Weng, X. Wu, X. Tang, P. Zhou, J. Zhou, S. Zhuo, Deciphering the formation process and electrochemical behavior of novel P2/O3 biphasic layered cathode with long cycle life for sodium-ion batteries, Journal of Power Sources 560 (2023) 232686. https://doi.org/https://doi.org/10.1016/j.jpowsour.2023.232686.

[38] X. Gao, H. Liu, H. Chen, Y. Mei, B. Wang, L. Fang, M. Chen, J. Chen, J. Gao, L. Ni, L. Yang, Y. Tian, W. Deng, R. Momen, W. Wei, L. Chen, G. Zou, H. Hou, Y.-M. Kang, X. Ji, Cationic-potential tuned biphasic layered cathodes for stable desodiation/sodiation, Science Bulletin 67(15) (2022) 1589-1602. https://doi.org/https://doi.org/10.1016/j.scib.2022.06.024.

[39] P. Zhou, Z. Che, J. Liu, J. Zhou, X. Wu, J. Weng, J. Zhao, H. Cao, J. Zhou, F. Cheng, High-entropy P2/O3 biphasic cathode materials for wide-temperature rechargeable sodium-ion batteries, Energy Storage Materials 57 (2023) 618-627. https://doi.org/https://doi.org/10.1016/j.ensm.2023.03.007.

[40] J. Mu, T. Cai, W. Dong, C. Zhou, Z. Han, F. Huang, Biphasic high-entropy layered oxide as a stable and high-rate cathode for sodium-ion batteries, Chemical Engineering Journal 471 (2023) 144403. https://doi.org/https://doi.org/10.1016/j.cej.2023.144403.

[41] S. Guo, P. Liu, H. Yu, Y. Zhu, M. Chen, M. Ishida, H. Zhou, A layered P2-and O3-type composite as a high-energy cathode for rechargeable sodium-ion batteries, Angewandte Chemie International Edition 54(20) (2015) 5894-5899. https://doi.org/10.1002/anie.201411788.

[42] H. Wang, Q. Liu, Y. Liu, Multi-ion doped P2/O3 biphasic layered oxides cathodes $Na_xNi_{0.2}Mn_{0.55}Cu_{0.14}Ti_yZn_zO_2$ for sodium-ion batteries, Journal of Alloys and Compounds 962 (2023) 171053. https://doi.org/https://doi.org/10.1016/j.jallcom.2023.171053.

[43] Y. Ding, S. Wang, Y. Sun, Q. Liu, Q. An, H. Guo, Layered cathode-$Na_{0.67}Li_{0.15}Ni_{0.18}Mg_{0.02}Mn_{0.8}O_2$ with P2/O3 hybrid phase for high-performance Na-ion batteries, Journal of Alloys and Compounds 939 (2023) 168780. https://doi.org/https://doi.org/10.1016/j.jallcom.2023.168780.

[44] M.A. Khan, D. Han, G. Lee, Y.-I. Kim, Y.-M. Kang, P2/O3 phase-integrated $Na_{0.\,7}MnO_2$ cathode materials for sodium-ion rechargeable batteries, Journal of Alloys and Compounds 771 (2019) 987-993. https://doi.org/10.1016/j.jallcom.2018.09.033.

[45] A.A. Coelho, TOPAS-Academic: An optimization program integrating computer algebra and crystallographic objects written in C++ J, Journal of Applied Crystallography 51 (2018) 210-218. https://doi.org/10.1107/S1600576718000183.

[46] L. Yang, J.M.L. del Amo, Z. Shadike, S.-M. Bak, F. Bonilla, M. Galceran, P.K. Nayak, J.R. Buchheim, X.-Q. Yang, T. Rojo, P. Adelhelm, A Co- and Ni-Free P2/O3 Biphasic Lithium Stabilized Layered Oxide for Sodium-Ion Batteries and its Cycling Behavior, Advanced Functional Materials 30(42) (2020) 2003364. https://doi.org/https://doi.org/10.1002/adfm.202003364.

[47] C. Chen, W. Huang, Y. Li, M. Zhang, K. Nie, J. Wang, W. Zhao, R. Qi, C. Zuo, Z. Li, H. Yi, F. Pan, P2/O3 biphasic Fe/Mn-based layered oxide cathode with ultrahigh capacity and great cyclability for sodium ion batteries, Nano Energy 90 (2021) 106504. https://doi.org/https://doi.org/10.1016/j.nanoen.2021.106504.

[48] J.H. Stansby, M. Avdeev, H.E.A. Brand, E. Gonzalo, N.E. Drewett, N. Ortiz-Vitoriano, N. Sharma, T. Rojo, Biphasic P2/O3-$Na_{2/3}Li_{0.18}Mn_{0.8}Fe_{0.2}O_2$: a structural investigation, Dalton Transactions 50(4) (2021) 1357-1365. https://doi.org/10.1039/D0DT03351K.

[49] A.K. Paidi, W.B. Park, P. Ramakrishnan, S.-H. Lee, J.-W. Lee, K.-S. Lee, H. Ahn, T. Liu, J. Gim, M. Avdeev, M. Pyo, J.I. Sohn, K. Amine, K.-S. Sohn, T.J. Shin, D. Ahn, J. Lu, Unravelling the Nature of the Intrinsic Complex Structure of Binary-Phase Na-Layered Oxides, Advanced Materials 34(29) (2022) 2202137. https://doi.org/https://doi.org/10.1002/adma.202202137.

[50] R. Berthelot, D. Carlier, C. Delmas, Electrochemical investigation of the P2–Na_xCoO_2 phase diagram, Nature Materials 10(1) (2011) 74-80. https://doi.org/10.1038/nmat2920.

[51] D.H. Lee, J. Xu, Y.S. Meng, An advanced cathode for Na-ion batteries with high rate and excellent structural stability, Physical Chemistry Chemical Physics 15(9) (2013) 3304-3312. https://doi.org/10.1039/C2CP44467D.

[52] P.-F. Wang, H.-R. Yao, X.-Y. Liu, Y.-X. Yin, J.-N. Zhang, Y. Wen, X. Yu, L. Gu, Y.-G. Guo, Na^+/vacancy disordering promises high-rate Na-ion batteries, Science Advances 4(3) (2018) eaar6018. https://doi.org/doi:10.1126/sciadv.aar6018.

[53] K. Momma, F. Izumi, VESTA 3 for three-dimensional visualization of crystal, volumetric and morphology data, Journal of Applied Crystallography 44(6) (2011) 1272-1276. https://doi.org/doi:10.1107/S0021889811038970.

[54] W. Kang, D.Y.W. Yu, P.-K. Lee, Z. Zhang, H. Bian, W. Li, T.-W. Ng, W. Zhang, C.-S. Lee, P2-Type $Na_xCu_{0.15}Ni_{0.20}Mn_{0.65}O_2$ Cathodes with High Voltage for High-Power and Long-Life Sodium-Ion Batteries, ACS Applied Materials & Interfaces 8(46) (2016) 31661-31668. https://doi.org/10.1021/acsami.6b10841.

[55] J. Chastain, R.C. King Jr, Handbook of X-ray photoelectron spectroscopy, 1992.

[56] S. Hüfner, Photoelectron spectroscopy: principles and applications, Springer Science & Business Media2013.

[57] X.-H. Zhang, W.-L. Pang, F. Wan, J.-Z. Guo, H.-Y. Lü, J.-Y. Li, Y.-M. Xing, J.-P. Zhang, X.-L. Wu, P2–$Na_{2/3}Ni_{1/3}Mn_{5/9}Al_{1/9}O_2$ Microparticles as Superior Cathode Material for Sodium-Ion Batteries: Enhanced Properties and Mechanism via Graphene Connection, ACS Applied Materials & Interfaces 8(32) (2016) 20650-20659. https://doi.org/10.1021/acsami.6b03944.

[58] G. Singh, N. Tapia-Ruiz, J.M. Lopez del Amo, U. Maitra, J.W. Somerville, A.R. Armstrong, J. Martinez de Ilarduya, T. Rojo, P.G. Bruce, High Voltage Mg-Doped $Na_{0.67}Ni_{0.3-x}Mg_xMn_{0.7}O_2$ (x = 0.05, 0.1) Na-Ion Cathodes with Enhanced Stability and Rate Capability, Chemistry of Materials 28(14) (2016) 5087-5094. https://doi.org/10.1021/acs.chemmater.6b01935.

[59] P. Ma, W. Kang, Y. Wang, D. Cao, L. Fan, D. Sun, Binary metal co-substituted P2-type $Na_{0.67}Mn_{0.7}Cu_{0.15}Ni_{0.15}O_2$ microspheres as robust cathode for high-power sodium ion battery, Applied Surface Science 529 (2020) 147105. https://doi.org/https://doi.org/10.1016/j.apsusc.2020.147105.

[60] R. Li, Y. Liu, Z. Wang, J. Li, A P2/O3 biphasic cathode material with highly reversibility synthesized by Sn-substitution for Na-ion batteries, Electrochimica Acta 318 (2019) 14-22. https://doi.org/https://doi.org/10.1016/j.electacta.2019.06.020.

[61] Q. Liu, Z. Hu, M. Chen, C. Zou, H. Jin, S. Wang, S.-L. Chou, S.-X. Dou, Recent Progress of Layered Transition Metal Oxide Cathodes for Sodium-Ion Batteries, Small 15(32) (2019) 1805381. https://doi.org/https://doi.org/10.1002/smll.201805381.

[62] C. Hakim, H.D. Asfaw, R. Younesi, D. Brandell, K. Edström, I. Saadoune, Development of P2 or P2/P3 cathode materials for sodium-ion batteries by controlling the Ni and Mn contents in $Na_{0.7}Co_xMn_yNi_zO_2$ layered oxide, Electrochimica Acta 438 (2023) 141540. https://doi.org/https://doi.org/10.1016/j.electacta.2022.141540.

[63] Q.-C. Wang, Z. Shadike, X.-L. Li, J. Bao, Q.-Q. Qiu, E. Hu, S.-M. Bak, X. Xiao, L. Ma, X.-J. Wu, X.-Q. Yang, Y.-N. Zhou, Tuning Sodium Occupancy Sites in P2-Layered Cathode Material for Enhancing Electrochemical Performance, Advanced Energy Materials 11(13) (2021) 2003455. https://doi.org/10.1002/aenm.202003455.

[64] M. Bañobre-López, F. Rivadulla, R. Caudillo, M.A. López-Quintela, J. Rivas, J.B. Goodenough, Role of Doping and Dimensionality in the Superconductivity of Na_xCoO_2, Chemistry of Materials 17(8) (2005) 1965-1968. https://doi.org/10.1021/cm0500760.

[65] J. Molenda, D. Baster, M. Molenda, K. Świerczek, J. Tobola, Anomaly in the electronic structure of the Na_xCoO_{2-y} cathode as a source of its step-like discharge curve, Physical Chemistry Chemical Physics 16(28) (2014) 14845-14857. https://doi.org/10.1039/C3CP55223C.

[66] J. Molenda, D. Baster, A. Stokłosa, M.U. Gutowska, A. Szewczyk, R. Puźniak, K. Dybko, M. Szot, J. Tobola, Correlation between electronic and electrochemical properties of Na_xCoO_{2-y}, Solid State Ionics 268 (2014) 179-184. https://doi.org/https://doi.org/10.1016/j.ssi.2014.10.029.

[67] Y.-E. Zhu, X. Qi, X. Chen, X. Zhou, X. Zhang, J. Wei, Y. Hu, Z. Zhou, A P2-$Na_{0.67}Co_{0.5}Mn_{0.5}O_2$ cathode material with excellent rate capability and cycling stability for sodium ion batteries, Journal of Materials Chemistry A 4(28) (2016) 11103-11109. https://doi.org/10.1039/C6TA02845D.

[68] X. Qi, Y. Wang, L. Jiang, L. Mu, C. Zhao, L. Liu, Y.-S. Hu, L. Chen, X. Huang, Sodium-Deficient O3-$Na_{0.9}[Ni_{0.4}Mn_xTi_{0.6-x}]O_2$ Layered-Oxide Cathode Materials for Sodium-Ion Batteries, Particle & Particle Systems Characterization 33(8) (2016) 538-544. https://doi.org/https://doi.org/10.1002/ppsc.201500129.

[69] W. Weppner, R.A. Huggins, Determination of the Kinetic Parameters of Mixed-Conducting Electrodes and Application to the System Li_3Sb, Journal of the Electrochemical Society 124(10) (1977) 1569. https://doi.org/10.1149/1.2133112.

[70] Q. Yang, P.-F. Wang, J.-Z. Guo, Z.-M. Chen, W.-L. Pang, K.-C. Huang, Y.-G. Guo, X.-L. Wu, J.-P. Zhang, Advanced P2-$Na_{2/3}Ni_{1/3}Mn_{7/12}Fe_{1/12}O_2$ Cathode Material with Suppressed P2–O2 Phase Transition toward High-Performance Sodium-Ion Battery, ACS Applied Materials & Interfaces 10(40) (2018) 34272-34282. https://doi.org/10.1021/acsami.8b12204.

[71] G. Zhang, J. Li, Y. Fan, Y. Liu, P. Zhang, X. Shi, J. Ma, R. Zhang, Y. Huang, Suppressed P2–P2′ phase transition of Fe/Mn-based layered oxide cathode for high-performance sodium-ion batteries, Energy Storage Materials 51 (2022) 559-567. https://doi.org/https://doi.org/10.1016/j.ensm.2022.06.045.

[Supplementary Information]

Deciphering the role of optimal P2/O3 phase fraction in enhanced cyclability and specific capacity of layered oxide cathodes

Samriddhi Saxena[a], Manish Badole[a], Hari Narayanan Vasavan[a], Velaga Srihari[b],

Asish Kumar Das[a], Pratiksha Gami[a], Sonia Deswal[c], Pradeep Kumar[c], Sunil Kumar[a,*]

[a] *Department of Metallurgical Engineering and Materials Science, Indian Institute of Technology Indore, Simrol, 453552, India*

[b] *High Pressure & Synchrotron Radiation Physics Division, Bhabha Atomic Research Centre, Mumbai, 400085, India*

[c] *School of Physical Sciences, Indian Institute of Technology Mandi, Mandi, 175005, India*

[*] *E-mail: sunil@iiti.ac.in*

The stoichiometric amounts of the precursors were calculated using the following chemical reaction:

$$\frac{x}{2}Na_2CO_3 + 0.3C_4H_6NiO_4.4H_2O + C_4H_6MnO_4.4H_2O + 0.1Cu(NO_3)_2.3H_2O$$
$$\rightarrow \boldsymbol{Na_xMn_{0.60}Ni_{0.30}Cu_{0.10}O_2} + Byproducts$$

The following table summarizes the exact amounts of precursors (in g) for varying *x* to obtain 10g of the final product:

Table S1. Exact precursor amount for varying *x* to obtain 10g of the final product.

x	**Na_2CO_3**	**$C_4H_6NiO_4.4H_2O$**	**$C_4H_6NiO_4.4H_2O$**	**$Cu(NO_3)_2.3H_2O$**
0.80	3.9505	6.9563	13.7027	2.2513
0.85	4.1528	6.8824	13.5572	2.2272
0.90	4.3511	6.8104	13.4153	2.2040
0.95	4.5448	6.7396	13.2760	2.1812
1.00	4.7352	6.6704	13.1396	2.1588

Table S2. Fractions of different phases with varying calcination temperatures in NMNC-*x*

Composition	NMNC-0.80			NMNC-0.90			NMNC-1.00		
Calcination temperature (°C)	P3	P2	O3	P3	P2	O3	P3	P2	O3
700	100	0	0	100	0	0	100	0	0
750	100	0	0	100	0	0	100	0	0
800	54±1	29±1	17±1	7±1	44±1	49±1	24±2	0	76±2
850	0	94±1	6±1	0	62±2	38±2	0	18±2	82±2
900	0	86±2	13±2	0	45±1	54±1	0	11±2	89±2
950	0	73±2	27±2	0	11±1	89±1	0	0	100
1000	0	95±1	5±1	0	0	100	0	0	100

Tables S3-S7. Crystallographic parameters of biphasic NMNC-*x* obtained from Rietveld refinement of room temperature XRD data.

S3: *x* = 0.80

O3 (Space Group: $R\bar{3}m$)					
Atom	**x**	**y**	**z**	**Occupancy**	**Site**
Na1	0	0	1/2	0.80	3b
Mn/Ni/Cu	0	0	0	0.60/0.30/0.10	3a
O	0	0	0.26	1.00	6c
P2 (Space Group : $P6_3/mmc$)					
Atom	**x**	**y**	**z**	**Occupancy**	**Site**
Na1	2/3	1/3	1/4	0.50	2d
Na2	0	0	1/4	0.30	2b
Mn/Ni/Cu	0	0	0	0.60/0.30/0.10	2a
O	2/3	1/3	0.09	1.00	4f

S4: *x* = 0.85

O3 (Space Group: $R\bar{3}m$)					
Atom	**x**	**y**	**z**	**Occupancy**	**Site**
Na1	0	0	1/2	0.85	3b
Mn/Ni/Cu	0	0	0	0.60/0.30/0.10	3a
O	0	0	0.26	1.00	6c
P2 (Space Group : $P6_3/mmc$)					
Atom	**x**	**y**	**z**	**Occupancy**	**Site**
Na1	2/3	1/3	1/4	0.55	2d
Na2	0	0	1/4	0.30	2b
Mn/Ni/Cu	0	0	0	0.60/0.30/0.10	2a
O	2/3	1/3	0.09	1.00	4f

S5: *x* = 0.90

O3 (Space Group: $R\bar{3}m$)					
Atom	**x**	**y**	**z**	**Occupancy**	**Site**
Na1	0	0	1/2	0.90	3b
Mn/Ni/Cu	0	0	0	0.60/0.30/0.10	3a
O	0	0	0.26	1.00	6c
P2 (Space Group : $P6_3/mmc$)					
Atom	**x**	**y**	**z**	**Occupancy**	**Site**
Na1	2/3	1/3	1/4	0.55	2d
Na2	0	0	1/4	0.35	2b
Mn/Ni/Cu	0	0	0	0.60/0.30/0.10	2a
O	2/3	1/3	0.09	1.00	4f

S6: *x* = 0.95

O3 (Space Group: $R\bar{3}m$)					
Atom	**x**	**y**	**z**	**Occupancy**	**Site**

Na1	0	0	1/2	0.95	3b
Mn/Ni/Cu	0	0	0	0.60/0.30/0.10	3a
O	0	0	0.26	1.00	6c
P2 (Space Group : P6$_3$/mmc)					
Atom	**x**	**y**	**z**	**Occupancy**	**Site**
Na1	2/3	1/3	1/4	0.65	2d
Na2	0	0	1/4	0.30	2b
Mn/Ni/Cu	0	0	0	0.60/0.30/0.10	2a
O	2/3	1/3	0.09	1.00	4f

S7: *x* = 1.00

O3 (Space Group: R$\bar{3}$m)					
Atom	**x**	**y**	**z**	**Occupancy**	**Site**
Na1	0	0	1/2	1.00	3b
Mn/Ni/Cu	0	0	0	0.60/0.30/0.10	3a
O	0	0	0.26	1.00	6c
P2 (Space Group : P6$_3$/mmc)					
Atom	**x**	**y**	**z**	**Occupancy**	**Site**
Na1	2/3	1/3	1/4	0.70	2d
Na2	0	0	1/4	0.30	2b
Mn/Ni/Cu	0	0	0	0.60/0.30/0.10	2a
O	2/3	1/3	0.09	1.00	4f

Table S8. The chemical compositions of the as-prepared samples were measured by inductively coupled plasma atomic emission spectroscopy (ICP-AES).

Sample	**Nominal composition**	**Calculated composition**
	Na/ Mn/ Ni/ Cu	**Na/ Mn/ Ni/ Cu**
NMNC-0.80	0.80/ 0.60/ 0.30/ 0.10	0.791 /0.606 /0.296 /0.097
NMNC-0.85	0.85/ 0.60 /0.30 /0.10	0.839 /0.604 /0.294 /0.096
NMNC-0.90	0.90 /0.60 /0.30 /0.10	0.892 /0.605 /0.298 /0.098
NMNC-0.95	0.95 /0.60 /0.30 /0.10	0.937 /0.604 /0.297 /0.094
NMNC-1.00	1.00 /0.60 /0.30 /0.10	0.986 /0.603 /0.299 /0.098

Table S9. Comparison of specific capacity and cyclability for various biphasic cathode materials for sodium-ion batteries.

Material	**Voltage Range vs. Na^+/Na**	**Capacity (0.1C, $mAh\ g^{-1}$)**	**Capacity retention, cycles, C-rate**
P2/O3 $Na_{0.736}Ni_{0.264}Mg_{0.1}Mn_{0.636}O_2$ [1]	2.0–4.3 V	130	73.1%, 200 cycles, 1C
P2/O3 $Na_{0.80}Li_{0.13}Ni_{0.20}Fe_{0.10}Mn_{0.57}O_2$ [2]	2.0–4.5 V	181	89.6%, 100 cycles, 1C
P2/O3 $Na_{0.67}Li_{0.15}Ni_{0.18}Mg_{0.02}Mn_{0.8}O_2$ [3]	1.5–4.2 V	160	70%, 100 cycles, 0.1C
P2/O3 $Na_{0.76}Ni_{0.33}Mn_{0.50}Fe_{0.10}Ti_{0.07}O_2$ [4]	2.2–4.3 V	160	79.2%, 100 cycles, 1C
P2/O3 $Li_{0.2}Na_{0.8}Ni_{0.33}Mn_{0.67}O_2$ [5]	2.0–4.3 V	132.5	80.1%, 120 cycles, 1C
Heterostructured coating of O3-$NaNi_{0.5}Mn_{0.5}O_2$ with P2-$Na_{2/3}MnO_2$ [6]	2.0–4.3 V	141.4	85.3%, 150 cycles, 1C
P2/O3 $Na_{0.85}Ni_{0.34}Mn_{0.33}Ti_{0.33}O_2$ [7]	2.2–4.4 V	126.6	80.6%, 200 cycles, 1C
P2/O3 $Na_{0.67}Ni_{0.4}Co_{0.2}Mn_{0.4}O_2$ [8]	1.5–4.2 V	150	81%, 100 cycles, 0.1C
P2/O3 $Na_{0.80}Mn_{0.60}Ni_{0.30}Cu_{0.10}O_2$ (***This work***)	2.0–4.2 V	147.6	92%, 200 cycles, 1C
P2/O3 $Na_{1.00}Mn_{0.60}Ni_{0.30}Cu_{0.10}O_2$ (***This work***)	2.0–4.2 V	187.6	91%, 200 cycles, 1C

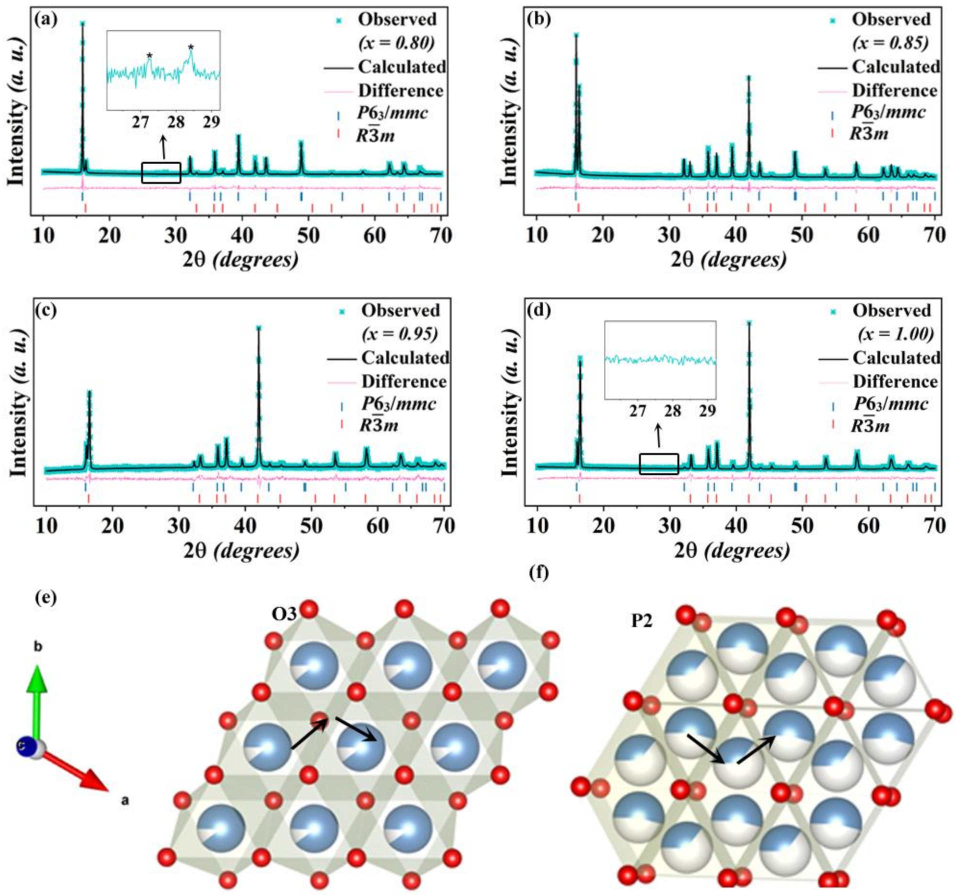

Fig. S1. Rietveld refinement profiles of XRD data for NMNC-*x* samples (a) *x* = 0.80 (inset shows the presence of Na-ion vacancy ordering peaks at 27.2° and 28.4° marked by *), (b) *x* = 0.85, (c) *x* = 0.95, and (d) *x* = 1.00 (inset shows the absence of Na-ion vacancy ordering peaks at 27.2° and 28.4°). (e) Crystal structures of the O3 and P2 phases visualized along the *c*-axis illustrating the Na-ion migration paths (represented by arrows) in the O3 phase through a tetrahedron between adjacent octahedra and in the P2 phase directly into the adjacent prisms.

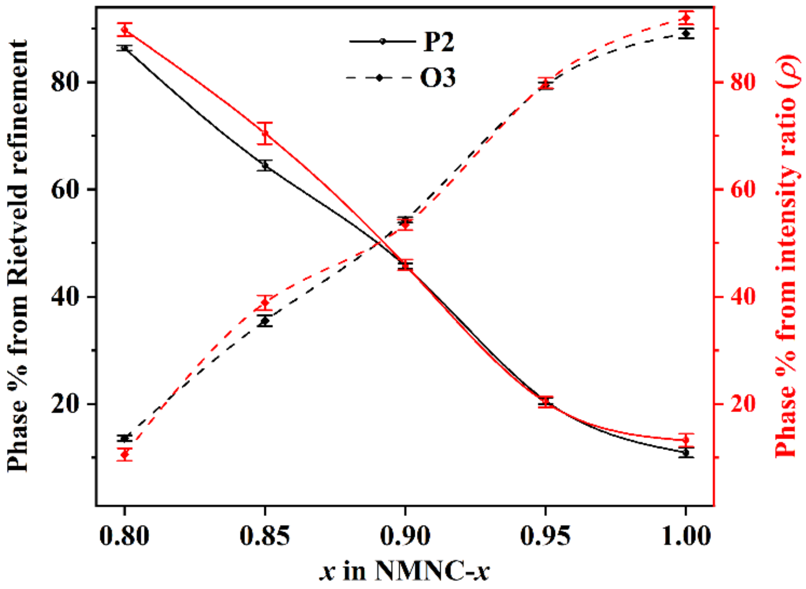

Fig. S2. Relation between the phase percentage calculated by the Rietveld refinement method (black) and that estimated by the intensity method (red) for the P2 and O3 phases.

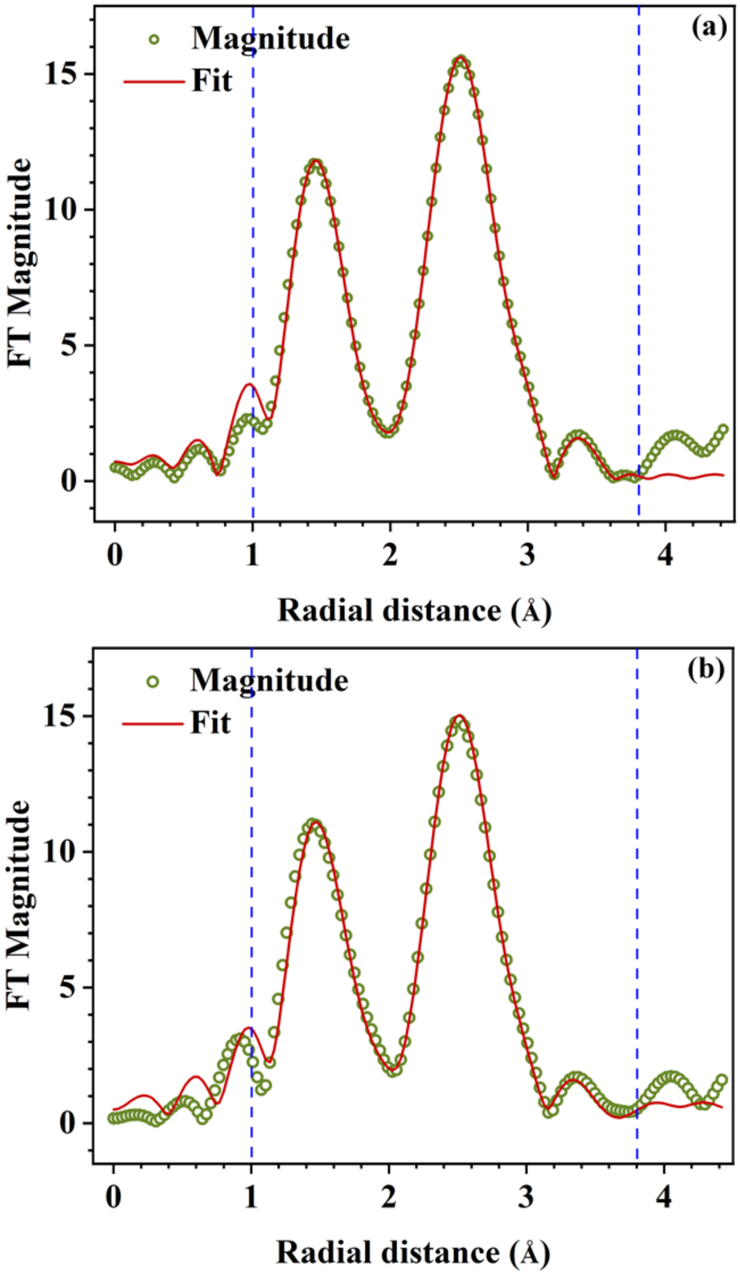

Fig. S3. Fourier transformation of the EXAFS spectra along with the fitting profiles (fitting range of 1–3.8 Å) of (a) NMNC-0.80 and (b) NMNC-1.00 at the Mn K-edge.

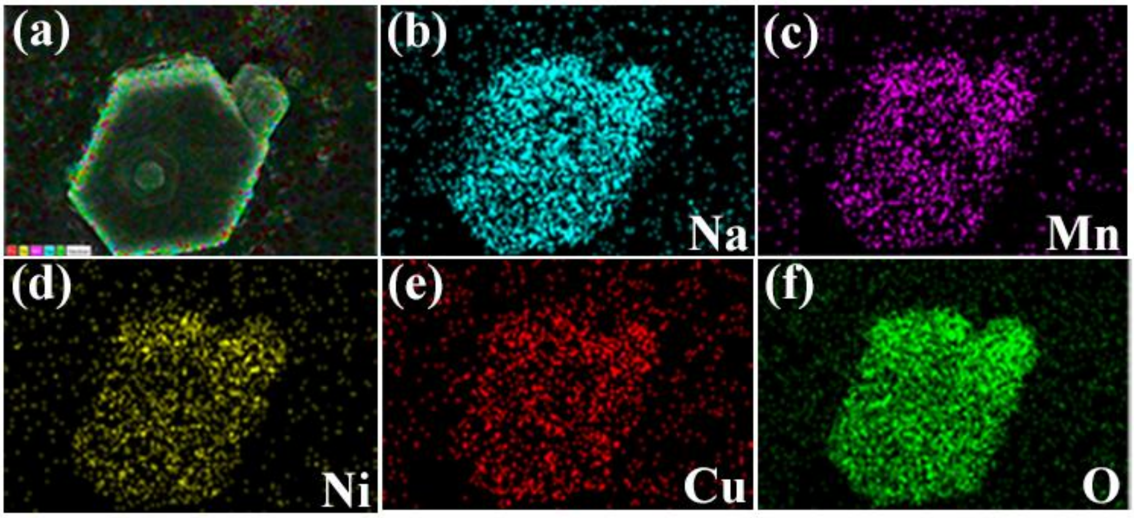

Fig. S4. (a-f) Elemental mapping of NMNC-0.90 indicating uniform distribution of constituent elements (Na, Mn, Ni, Cu, and O).

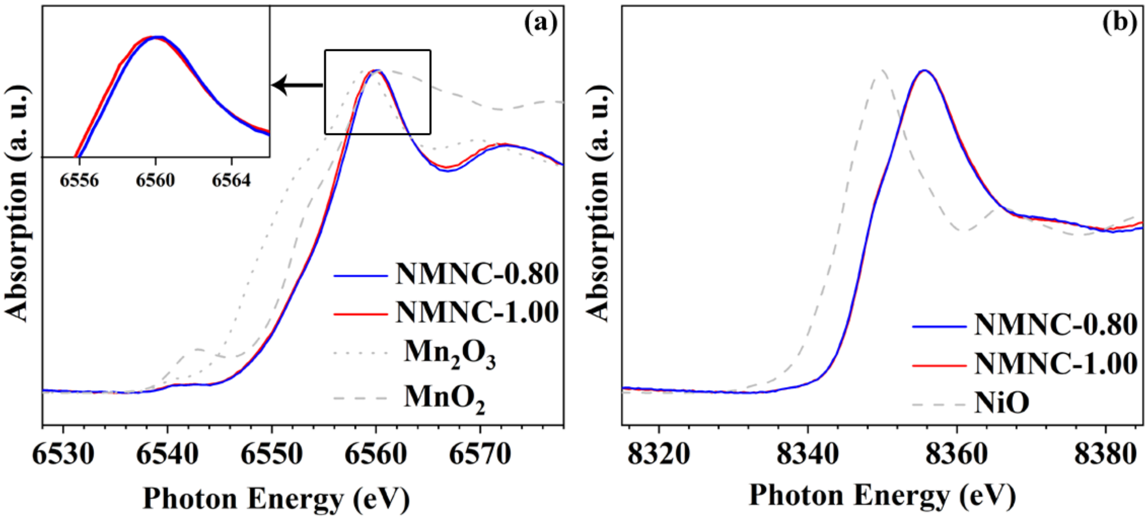

Fig. S5. XANES spectra at (a) Mn K-edge (inset shows an enlarged view) and (b) Ni K-edge of NMNC-0.80 & NMNC-1.00.

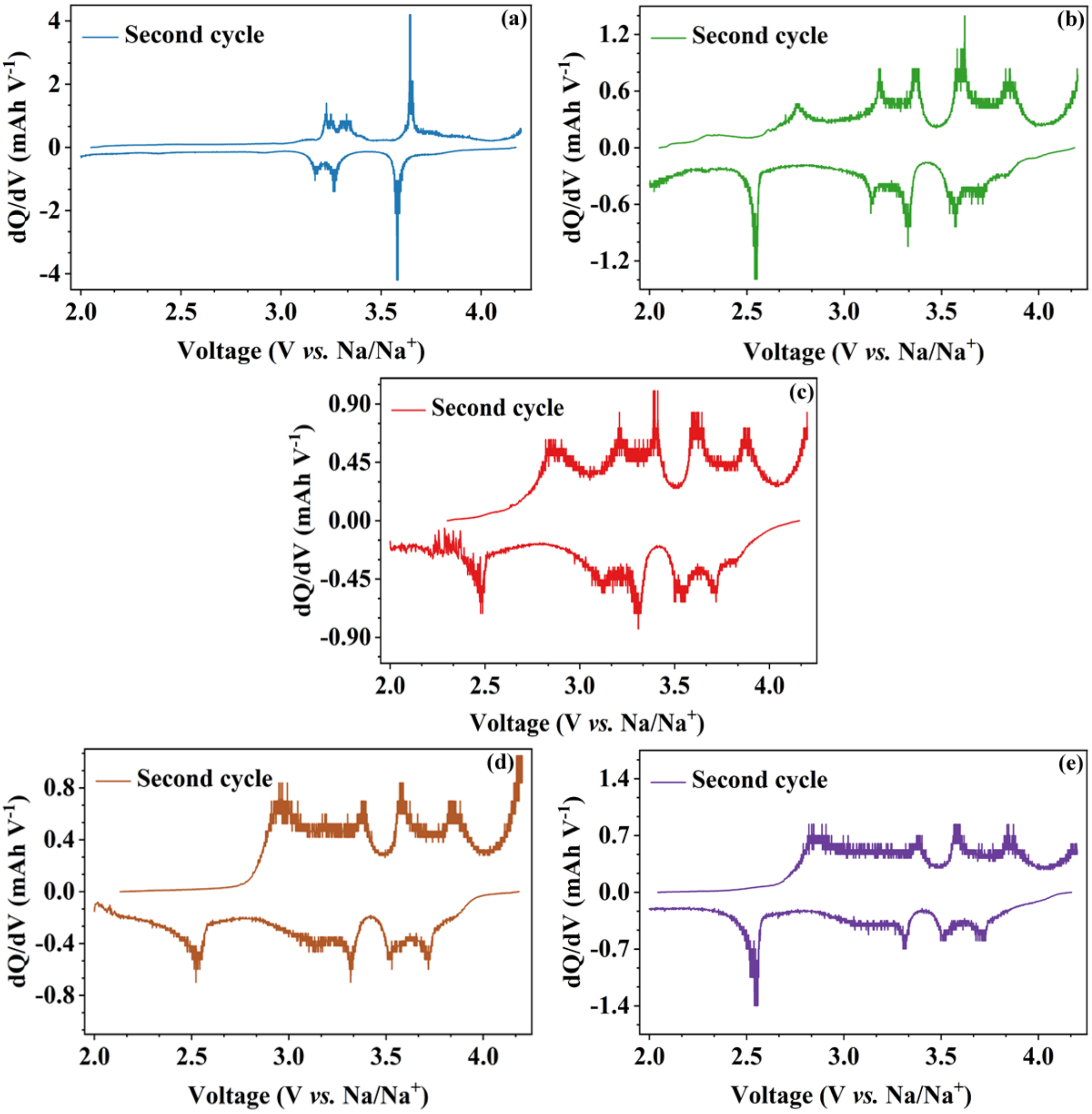

Fig. S6. dQ/dV *vs.* V plots of (a) NMNC-0.80, (b) NMNC-0.85, (c) NMNC-0.90, (d) NMNC-0.95, and (e) NMNC-1.00.

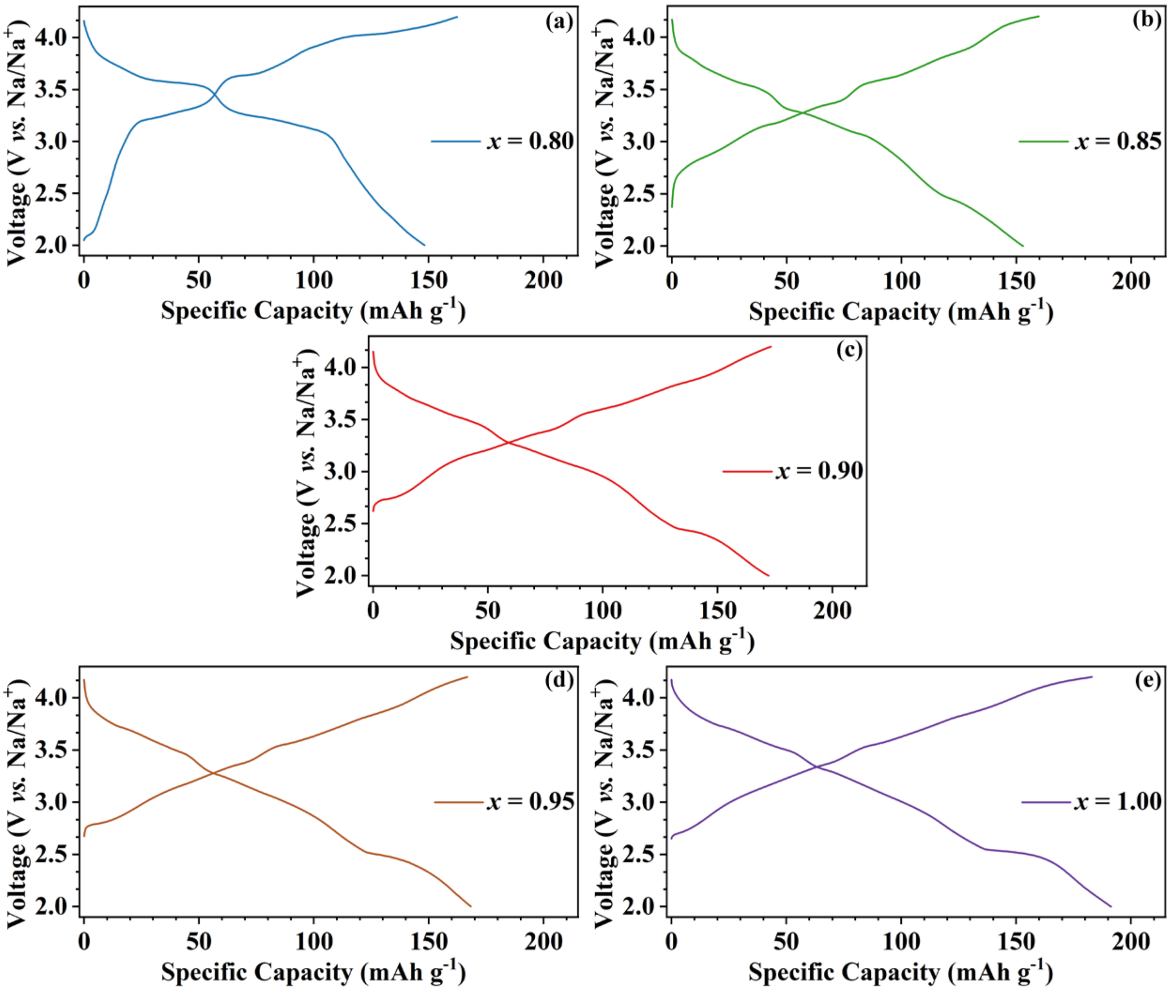

Fig. S7. The first charge-discharge cycle of (a) NMNC-0.80, (b) NMNC-0.85, (c) NMNC-0.90, (d) NMNC-0.95, and (e) NMNC-1.00 at 0.1C.

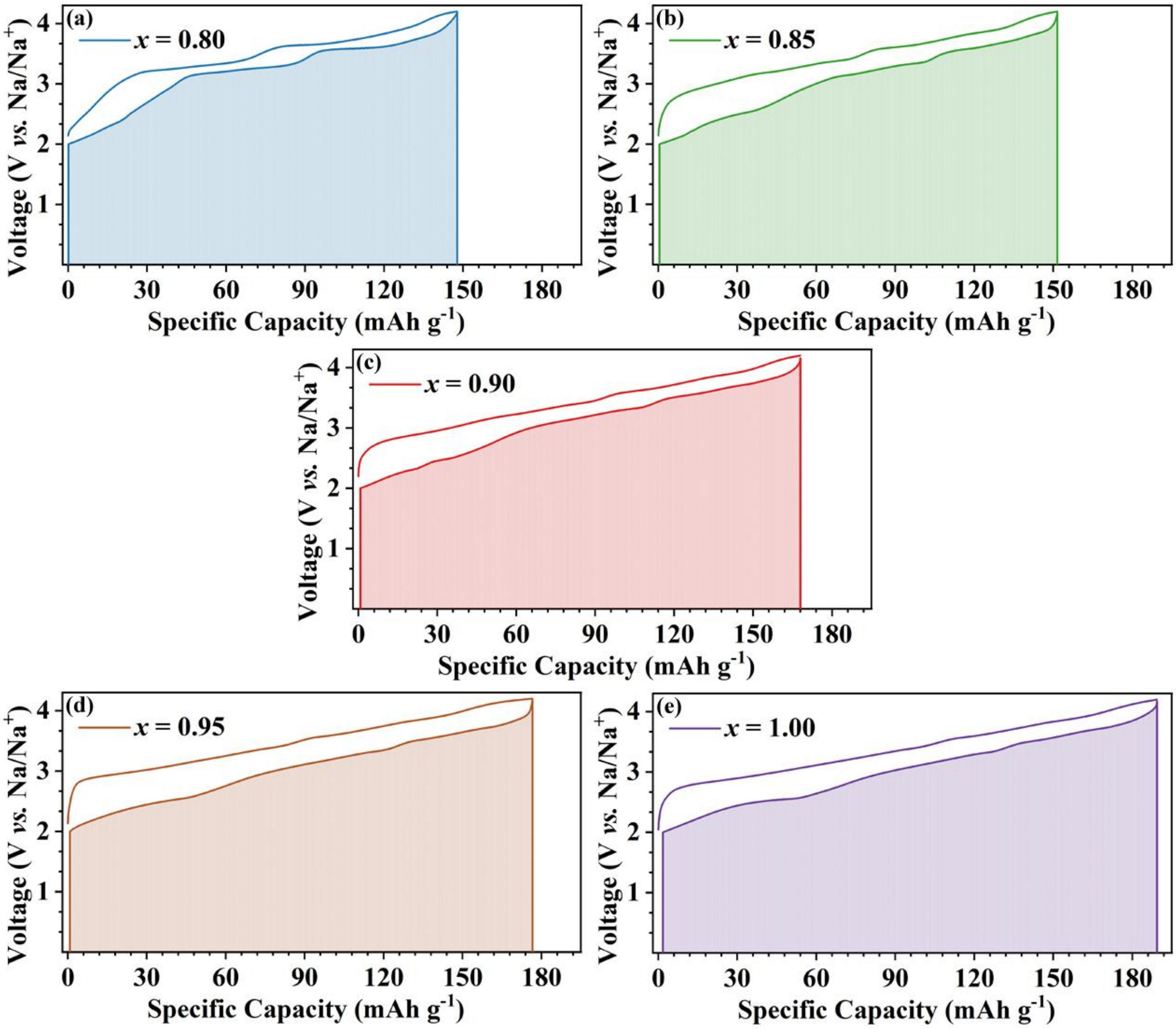

Fig. S8. The energy efficiency curves of (a) NMNC-0.80, (b) NMNC-0.85, (c) NMNC-0.90, (d) NMNC-0.95, and (e) NMNC-1.00 at 0.1C.

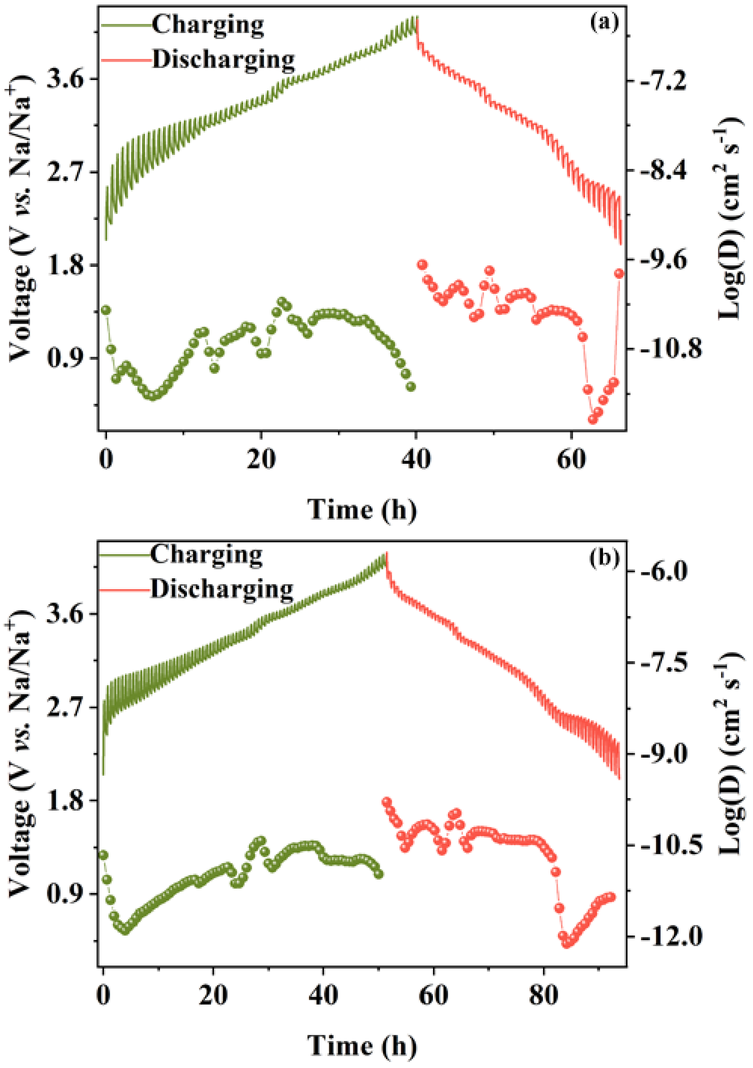

Fig. S9. GITT profile of (a) NMNC-0.85 and (b) NMNC-0.95 electrode along with diffusion coefficient of Na$^+$ at different stages during charge-discharge.

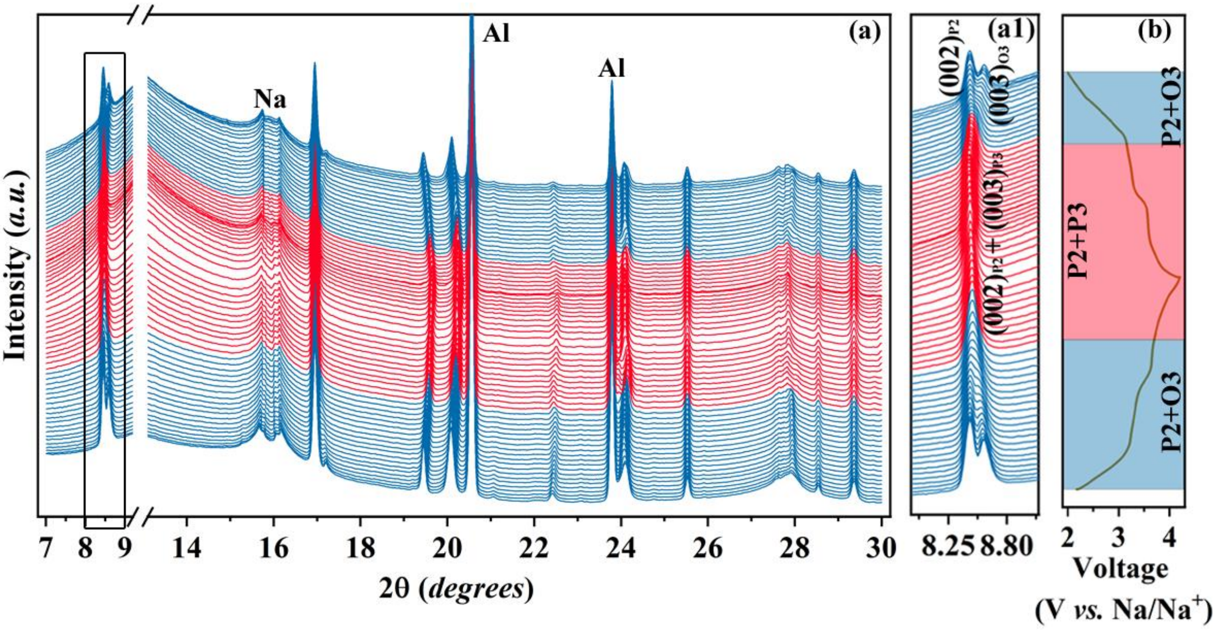

Fig. S10. (a) *Operando* Synchrotron XRD pattern of NMNC-0.80 sample at different states of charge between 4.2 and 2.0 V during charging and discharging at 0.1C. (a1) Enlarged view of (002) peak of P2 and (003) peak of (003) showing phase transformation of O3 to P3 and change in *c*-lattice parameter. (b) Corresponding GCD curve showing various states of charge and discharge.

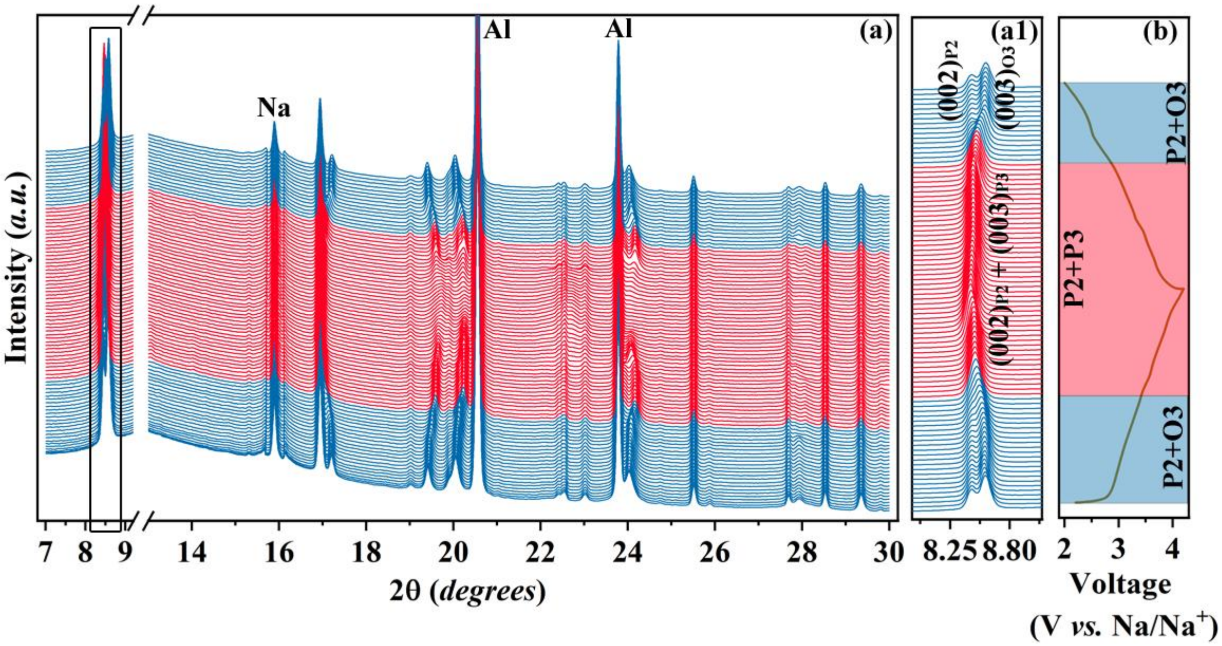

Fig. S11. (a) *Operando* Synchrotron XRD pattern of NMNC-1.00 sample at different states of charge between 4.2 and 2.0 V during charging and discharging at 0.1C. (a1) Enlarged view of (002) peak of P2 and (003) peak of (003) showing phase transformation of O3 to P3 and change in the *c*-lattice parameter. (b) Corresponding GCD curve showing various states of charge and discharge.

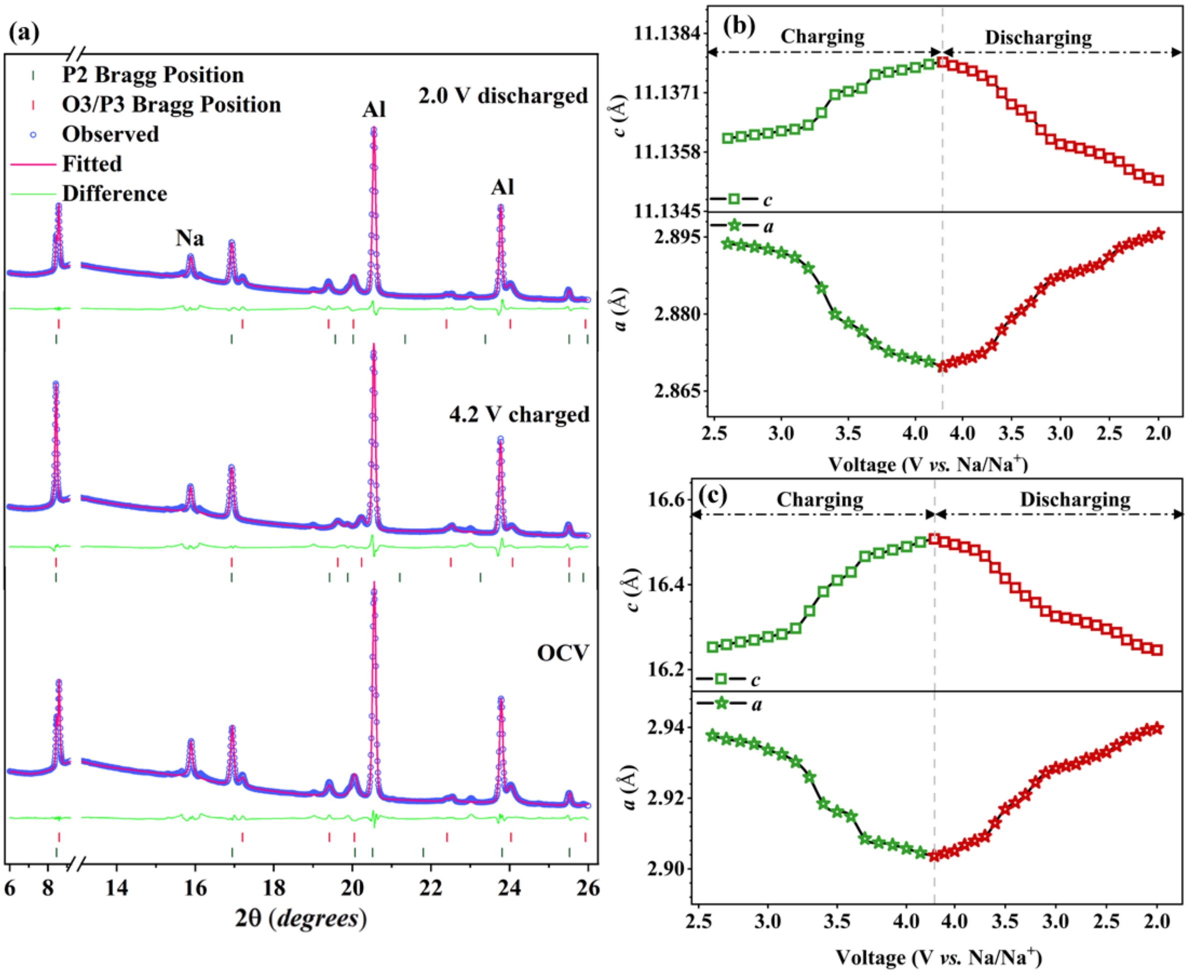

Fig. S12. (a) LeBail fitted profiles of *operando* Synchrotron XRD data at OCV ~ 2.6 V, 4.2 V, and 2.0 V for NMNC-0.80. Variation in lattice parameters of (b) P2 phase and (c) O3 phase during charging/ discharging.

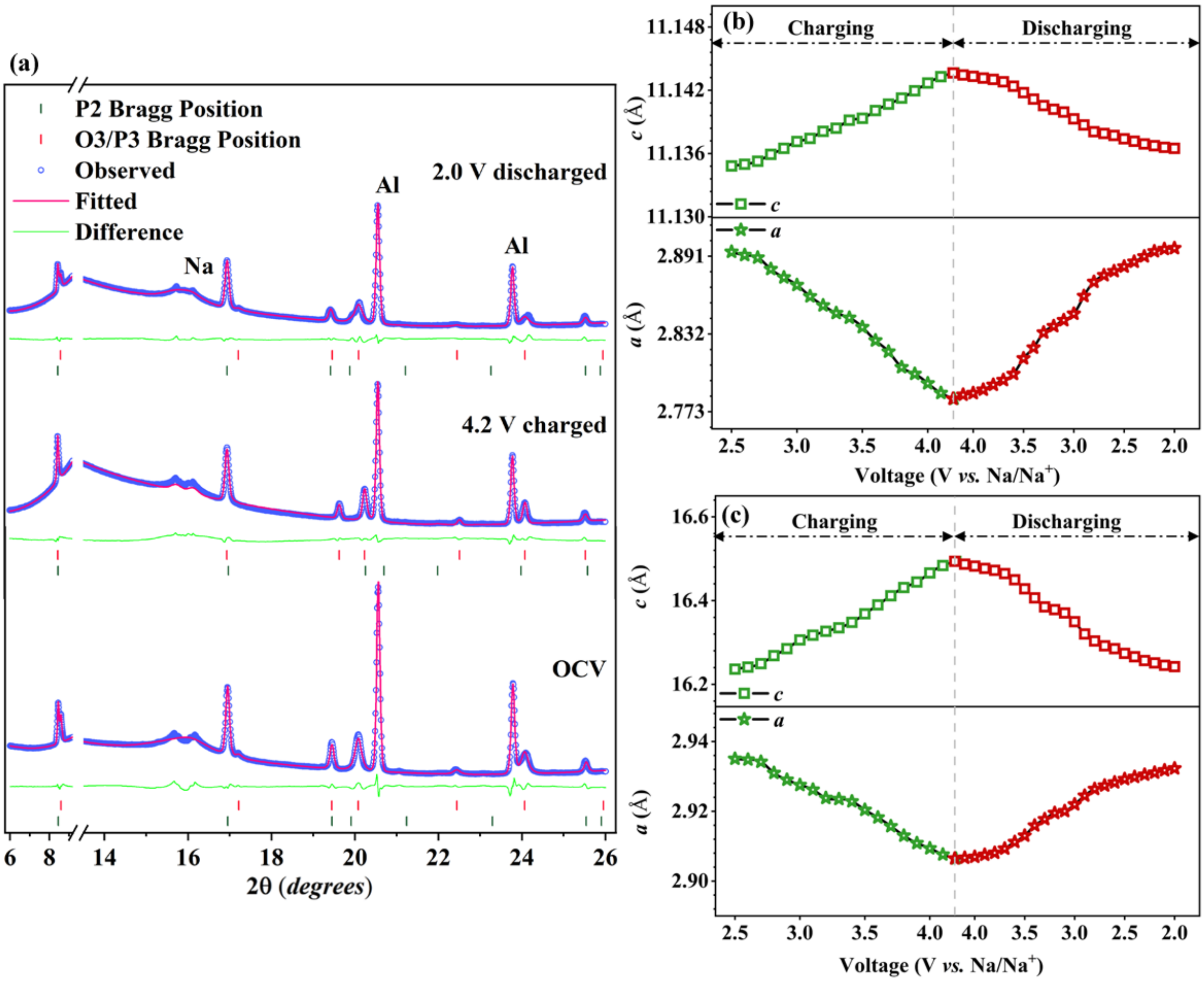

Fig. S13. (a) LeBail fitted profiles of *operando* Synchrotron XRD data at OCV ~ 2.5 V, 4.2 V, and 2.0 V for NMNC-1.00. Variation in lattice parameters of (b) P2 phase and (c) O3 phase during charging/ discharging.

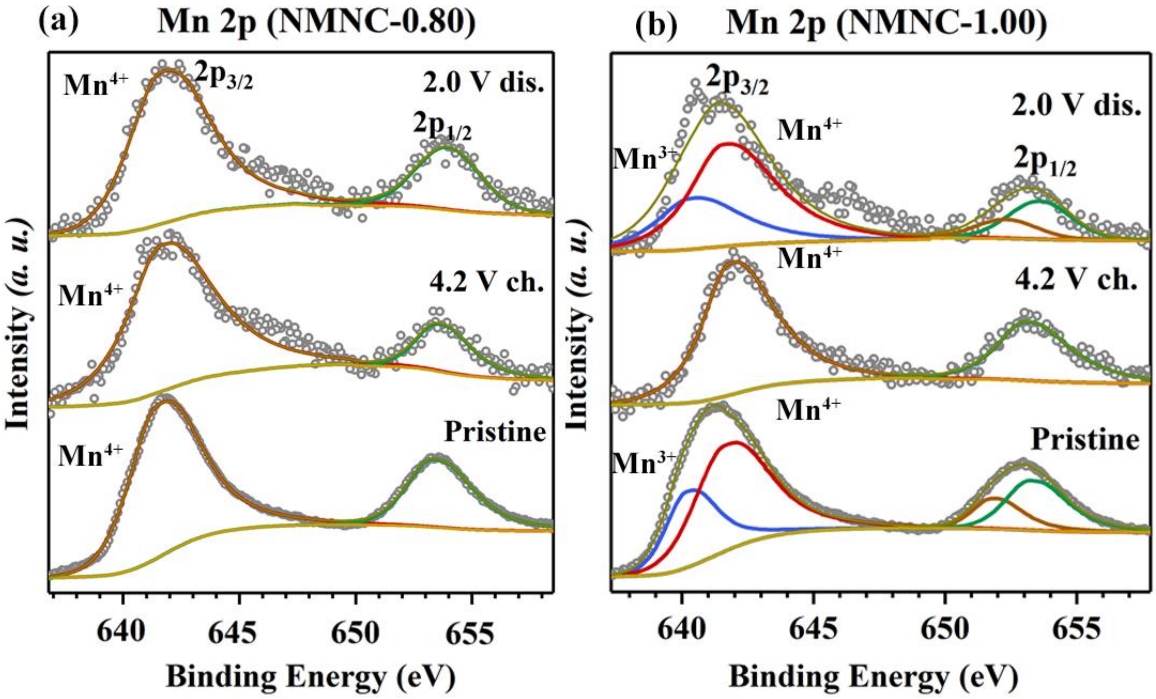

Fig. S14. Mn 2p spectra of (a) NMNC-0.80 and (b) NMNC-1.00 for Pristine, fully charged (4.2 V ch.), and fully discharged states (2.0 V dis.).

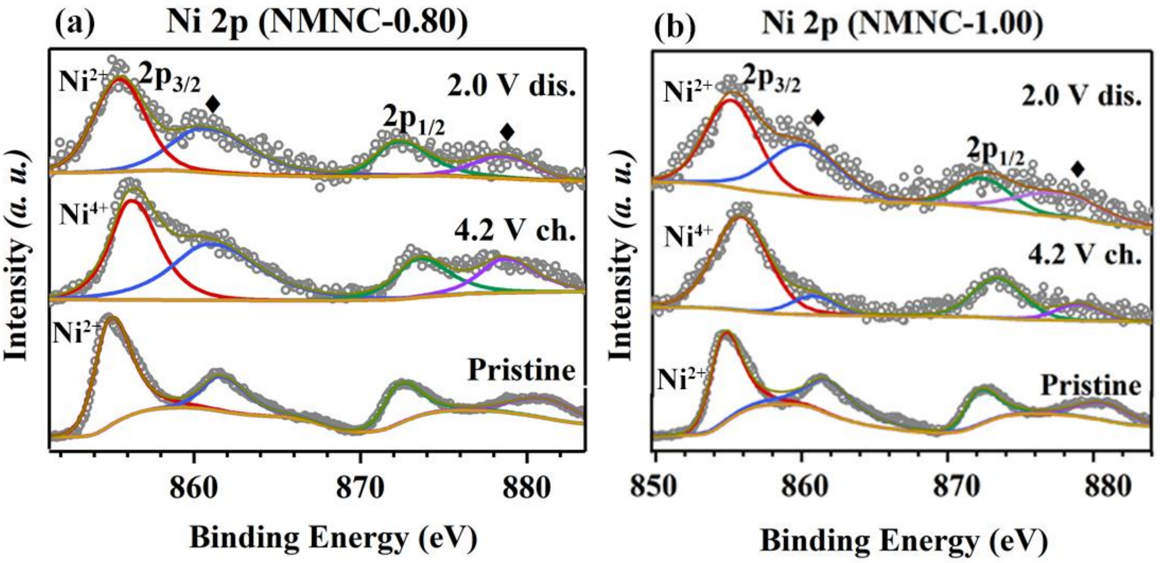

Fig. S15. Ni 2p spectra of (a) NMNC-0.80 and (b) NMNC-1.00 for Pristine, fully charged (4.2 V ch.), and fully discharged (2.0 V dis.) states.

References:

[1] L. Zhang, C. Guan, J. Zheng, H. Li, S. Li, S. Li, Y. Lai, Z. Zhang, Rational design of intergrowth P2/O3 biphasic layered structure with reversible anionic redox chemistry and structural evolution for Na-ions batteries, Science Bulletin 68(2) (2023) 180-191. https://doi.org/https://doi.org/10.1016/j.scib.2023.01.010.
[2] J. Feng, D. Fang, Z. Yang, J. Zhong, C. Zheng, Z. Wei, J. Li, A novel P2/O3 composite cathode toward synergistic electrochemical optimization for sodium ion batteries, J. Power Sources 553 (2023) 232292. https://doi.org/https://doi.org/10.1016/j.jpowsour.2022.232292.
[3] Y. Ding, S. Wang, Y. Sun, Q. Liu, Q. An, H. Guo, Layered cathode-$Na_{0.67}Li_{0.15}Ni_{0.18}Mg_{0.02}Mn_{0.8}O_2$ with P2/O3 hybrid phase for high-performance Na-ion batteries, J. Alloys Compd. 939 (2023) 168780. https://doi.org/https://doi.org/10.1016/j.jallcom.2023.168780.
[4] Z. Cheng, X.-Y. Fan, L. Yu, W. Hua, Y.-J. Guo, Y.-H. Feng, F.-D. Ji, M. Liu, Y.-X. Yin, X. Han, Y.-G. Guo, P.-F. Wang, A Rational Biphasic Tailoring Strategy Enabling High-Performance Layered Cathodes for Sodium-Ion Batteries, Angew. Chem. Int. Ed. 61(19) (2022) e202117728. https://doi.org/https://doi.org/10.1002/anie.202117728.
[5] J. Feng, S.-h. Luo, J. Cong, K. Li, S. Yan, Q. Wang, Y. Zhang, X. Liu, X. Lei, P.-q. Hou, Synthesis and electrochemical properties of Co-free P2/O3 biphasic $Na_{1-x}Li_xNi_{0.33}Mn_{0.67}O_2$ cathode material for sodium-ion batteries, J. Electroanal. Chem. 916 (2022) 116378. https://doi.org/https://doi.org/10.1016/j.jelechem.2022.116378.
[6] X. Liang, T.-Y. Yu, H.-H. Ryu, Y.-K. Sun, Hierarchical O3/P2 heterostructured cathode materials for advanced sodium-ion batteries, Energy Storage Mater. 47 (2022) 515-525. https://doi.org/https://doi.org/10.1016/j.ensm.2022.02.043.
[7] L. Yu, Z. Cheng, K. Xu, Y.-X. Chang, Y.-H. Feng, D. Si, M. Liu, P.-F. Wang, S. Xu, Interlocking biphasic chemistry for high-voltage P2/O3 sodium layered oxide cathode, Energy Storage Mater. 50 (2022) 730-739. https://doi.org/https://doi.org/10.1016/j.ensm.2022.06.012.
[8] X. Sun, X.-Y. Ji, H.-Y. Xu, C.-Y. Zhang, Y. Shao, Y. Zang, C.-H. Chen, Sodium insertion cathode material $Na_{0.67}[Ni_{0.4}Co_{0.2}Mn_{0.4}]O_2$ with excellent electrochemical properties, Electrochim. Acta 208 (2016) 142-147. https://doi.org/https://doi.org/10.1016/j.electacta.2016.04.067.